

REPORT DOCUMENTATION PAGE

Form Approved
OMB No. 0704-0188

Public reporting burden for this collection of information is estimated to average 1 hour per response, including the time for reviewing instructions, searching existing data sources, gathering and maintaining the data needed, and completing and reviewing this collection of information. Send comments regarding this burden estimate or any other aspect of this collection of information, including suggestions for reducing this burden to Department of Defense, Washington Headquarters Services, Directorate for Information Operations and Reports (0704-0188), 1215 Jefferson Davis Highway, Suite 1204, Arlington, VA 22202-4302. Respondents should be aware that notwithstanding any other provision of law, no person shall be subject to any penalty for failing to comply with a collection of information if it does not display a currently valid OMB control number. **PLEASE DO NOT RETURN YOUR FORM TO THE ABOVE ADDRESS.**

1. REPORT DATE (DD-MM-YYYY)		2. REPORT TYPE	3. DATES COVERED (From - To)		
4. TITLE AND SUBTITLE			5a. CONTRACT NUMBER		
			5b. GRANT NUMBER		
			5c. PROGRAM ELEMENT NUMBER		
6. AUTHOR(S)			5d. PROJECT NUMBER		
			5e. TASK NUMBER		
			5f. WORK UNIT NUMBER		
7. PERFORMING ORGANIZATION NAME(S) AND ADDRESS(ES)			8. PERFORMING ORGANIZATION REPORT NUMBER		
9. SPONSORING / MONITORING AGENCY NAME(S) AND ADDRESS(ES)			10. SPONSOR/MONITOR'S ACRONYM(S)		
			11. SPONSOR/MONITOR'S REPORT NUMBER(S)		
12. DISTRIBUTION / AVAILABILITY STATEMENT					
13. SUPPLEMENTARY NOTES					
14. ABSTRACT					
15. SUBJECT TERMS					
16. SECURITY CLASSIFICATION OF:			17. LIMITATION OF ABSTRACT	18. NUMBER OF PAGES	19a. NAME OF RESPONSIBLE PERSON
a. REPORT	b. ABSTRACT	c. THIS PAGE			19b. TELEPHONE NUMBER (include area code)

Interim Research Performance Report

22 December 2016

Award Number: N00014-12-10184

Turbulence Simulation of Laboratory Wind-Wave Interaction in High Winds and Upscaling to Ocean Conditions

Michael L. Banner

School of Mathematics and Statistics, The University of New South Wales, Sydney 2052, Australia
Tel : (+61-2) 9385-7064 fax: (+61-2) 9385-7123 email: m.banner@unsw.edu.au

Russel P. Morison

School of Mathematics and Statistics, The University of New South Wales, Sydney 2052, Australia;
Tel : (+61-2) 9385-7064 fax: (+61-2) 9385-7123 email: r.morison@unsw.edu.au

William L. Peirson

New College, UNSW Australia, Sydney, NSW 2052, Australia
Tel : (+61-2) 9381-1999 fax: (+61-2) 9385-1909 email: B.Peirson@newcollege.unsw.edu.au

Collaborating Partner: Peter P. Sullivan

National Center for Atmospheric Research, Boulder, CO, USA
Tel: 303-497-8953 fax: 303-497-8171 email: pps@ucar.edu

Executive Summary

Our LES modeling study of waves strongly forced by winds investigated air-sea fluxes characterized by strong air flow separation over a very steep wave field. We first investigated propagating steep wave forms with fixed shape where the dominant effect on momentum flux was found to be geometrical steepness not the fluid speed distribution along the boundary, which was previously thought to be an important factor. Adding a realistic surface wind drift current produced only a small increase in the mean wind profile, and a minor reduction in the form drag fraction. This supports recent theoretical perspectives that propose very differing mechanisms for flow separation over rigid surfaces compared with unsteady surfaces with a boundary slip velocity.

We investigated passive scalar fluxes. In turbulent flow over steep stationary roughness, the primary mechanism for momentum flux is via pressure drag resulting from flow separation. However, scalar fluxes are determined largely by viscous processes. We found that the momentum and scalar fluxes differ fundamentally in their dependence on surface properties and flow separation.

Strongly-forced wind seas are characterized by enhanced group modulation, as significant additional energy flux from the wind augments the hydrodynamic modulations. Using compact steep chirped wave packets, we investigated for the first time the influence of strong temporal and spatial modulation, which was found to introduce large transient separation events into the LES aerodynamics. These strong perturbations in the air flow separation penetrate to significant elevations above the waves and contribute large local spikes in the wave form drag that add significant contributions to the mean stress. These findings suggest that more refined knowledge and inclusion of modulational properties of the wave field might provide more accurate estimates of the drag coefficient.

Finally, we investigated the scope for upscaling these results to strongly forced ocean conditions where the wave spectral bandwidth is much broader. Overall, the fundamental aerodynamic behavior associated with modulation that we discovered in our LES study has a strong counterpart over shorter wave scales, and further detailed observational knowledge of their modulational properties appears warranted. Our simulations did not account for: long wave-short wave interactions which may impact strongly on surface fluxes; spray and large droplet production associated with breaking wave crests and even crest disintegration through shearing at the highest wind speeds.

LONG-TERM GOALS

Wind-wave interactions are of fundamental importance as they determine the sea surface drag and scalar exchange between the atmosphere and ocean. This is particularly important at high winds since air-sea fluxes substantially affect tropical cyclone (hurricane) formation and intensity. There is large uncertainty in the bulk momentum and heat surface exchange coefficients (C_d , C_k) derived from field observations and laboratory experiments for varying wind speed, wave age, swell amplitude and direction and in the presence of spray, with an even greater debate as to the underlying dynamical processes that couple the winds and waves. In this context, the overarching theme of this project is to identify the physical processes that couple winds in the marine atmospheric boundary layer and the underlying surface gravity wave field at high wind speeds and sea states.

This study is aimed at advancing fundamental understanding of air-sea interactions, which play a critical role in forecasting marine weather, ocean waves and upper ocean dynamics. Central to air-sea interaction mechanics is the coupling between turbulence in the surface layers of the marine boundary layers and the connecting surface gravity wave field, which determines the sea surface drag and the scalar exchange between the atmosphere and ocean. The emphasis of this effort is to refine present knowledge of the influence of wave breaking and complex sea surface topography in air-sea interactions. This includes a reduction in the present large uncertainty in measured values of the momentum and scalar exchange coefficients for wind speeds greater than 20 m/s by clarifying their dependence on various physical factors, including wind speed, wave age, wind-wave direction, wave spectral bandwidth, air flow separation and surface roughness.

OBJECTIVES

In this collaborative study, the UNSW team (Banner, Morison, Peirson) interacted closely with P. Sullivan at NCAR. Through email, skype conferencing and site visits by the UNSW PIs to NCAR, we built synergistically on our substantial accumulated expertise in sea surface processes and air-sea interaction. Our effort included adaptation and transfer of key laboratory observations and numerical simulations of steep non-breaking and breaking wave flows into Sullivan's NCAR LES flow domain, then performing increasingly refined simulations to optimise accuracy, followed by detailed analyses. The cases on which our effort was focused are not amenable to measurement or analysis for key details of their underlying flow physics. To illustrate, Fig. 1 shows measurements by PI Peirson and his collaborators in a large wind-wave facility. These data highlight the remarkable behavior of the wind stress as the dominant wave steepness (AK) increases. Initially, the wind stress decreases slightly, but increases rapidly above 0.19. The dominant wave breaking probability shows a similar trend. Such steep wave events can occur at sea during periods of very strong winds, which correspond to young wind sea conditions such as developing waves driven by gale force and stronger winds.

This project seeks to reconcile laboratory and field measurements of wind-wave interaction and surface drag in high to extreme winds, using turbulence resolving large-eddy simulations (LES). The recently published image sequence in figure 2 (Buckley and Veron, 2016) illustrates the strong changes in the wind structure over waves as the wind speed increases from <1 m/s to over 14 m/s above laboratory waves traveling at around 1 m/s. As the wind speed and wave steepness increase, the aerodynamic flow transitions from attached to separated, where the air velocity falls to zero relative to the wave crest speed, downwind of the wave crest. This signals a very strong change in the fluxes between wind and waves, as well as for other key air-sea fluxes such as gases, heat, and sea spray.

The basic science question we address is: what dynamical processes are operative and how confidently can we upscale these processes and measured statistics in small-scale laboratory experiments to high wind, open ocean conditions?

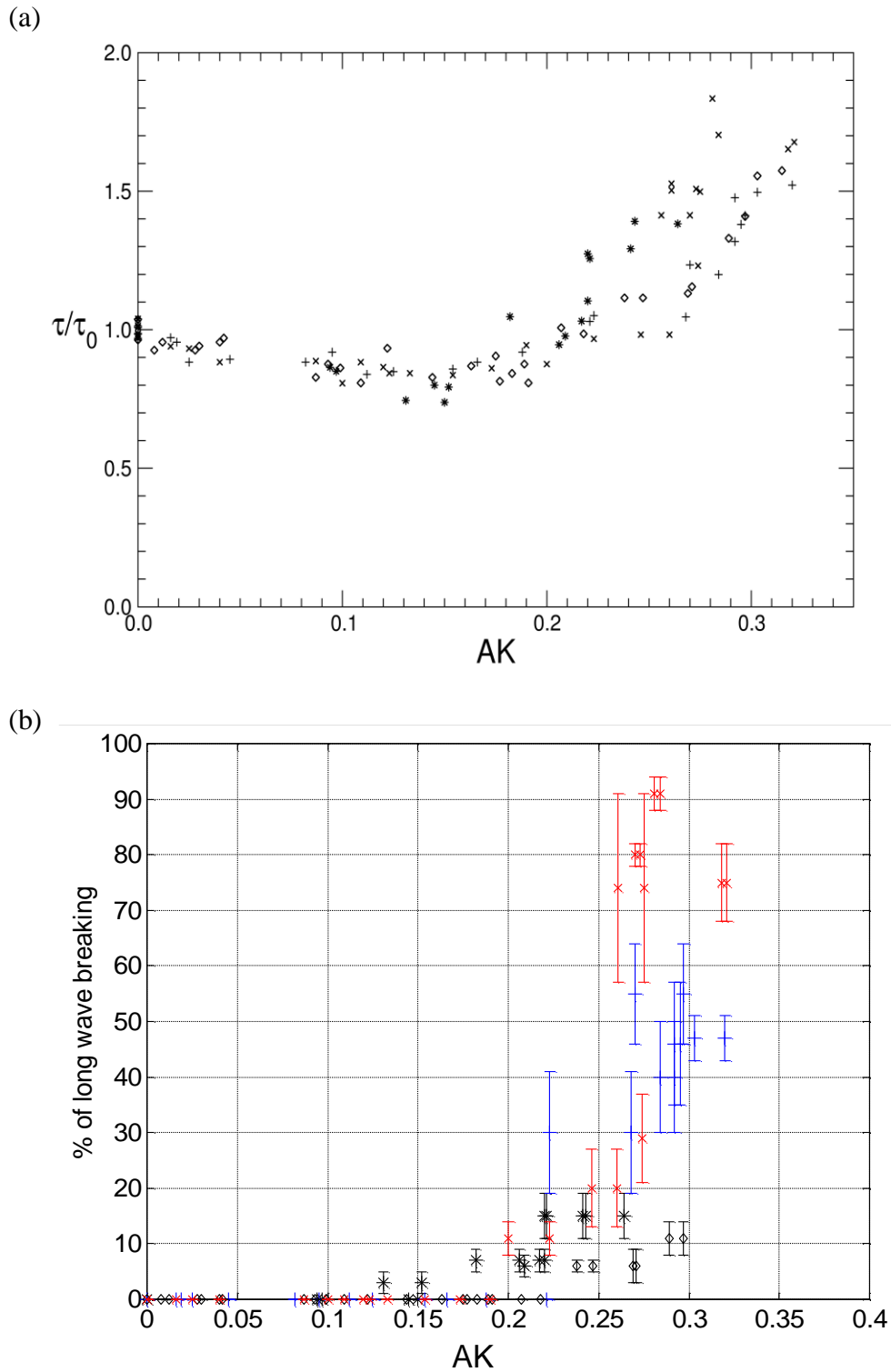


Figure 1. Panel (a) shows total wind stress normalized by total wind stress measured in the absence of the dominant wave (wind-rippled surface), as a function of the dominant wave steepness AK . Panel (b) shows the breaking probability of the dominant waves as a function of their steepness AK . Note that at given value of AK , the breaking probability increases with wave frequency and wind forcing strength. Cases shown in both panels are: * $U=6\text{ms}^{-1}$, $f_{DW}=2.0\text{Hz}$; + $U=8\text{ms}^{-1}$, $f_{DW}=1.6\text{Hz}$; diamonds $U=6\text{ms}^{-1}$, $f_{DW}=1.4\text{Hz}$; \times $U=10\text{ms}^{-1}$, $f_{DW}=1.4\text{Hz}$.

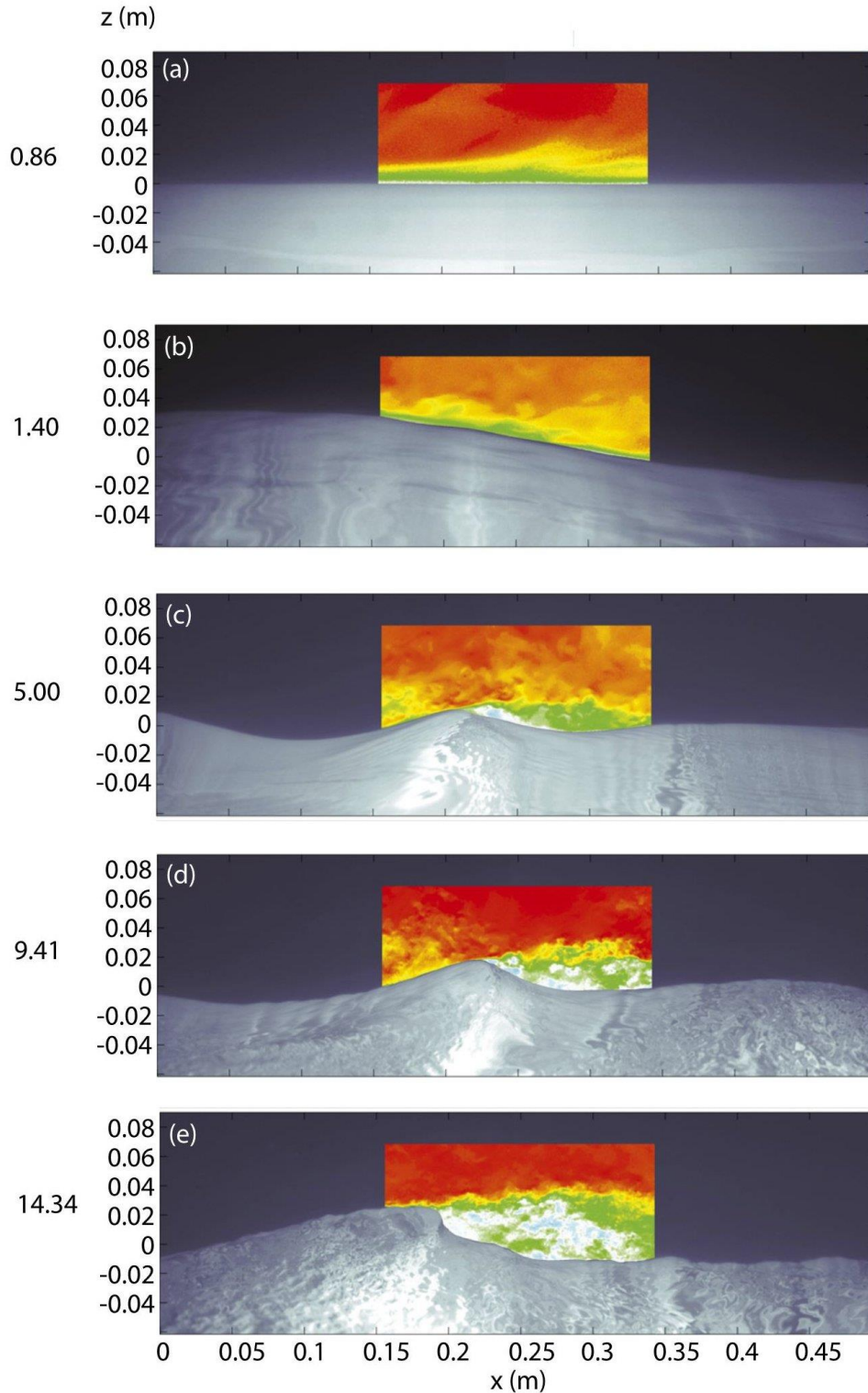


Figure 2. Instantaneous velocity fields of u/U_{10} from Figure 5 in Buckley & Veron (2016): the wind speed in m/s and the vertical scale is shown to the left of each panel. This illustrates the strong changes in the wind structure over waves as the wind speed increases from <1 m/s to over 14 m/s above laboratory waves traveling at around 1 m/s. The aerodynamic flow transitions from attached to separated, where the air velocity falls to zero relative to the wave crest speed, downwind of the wave crest. This signals a very strong change in the fluxes between wind and waves, as well as for other key air-sea fluxes such as gases, heat, and sea spray.

APPROACH

For this collaborative project, LES of the airflow over steep and breaking waves was carried out over a range of wind speeds and wave conditions matching selected laboratory wind-wave experiments. Simulation data were analyzed extensively to generate flow visualization, bulk mean flow and turbulence statistics and surface drag, and are compared with the observed experimental results. This detailed comparison of simulation and experimental results is used to identify the fundamental dynamical processes in wind-wave interaction, viz., flow separation and reattachment, impacts of surface roughness and swell steepness as a function of non-breaking and breaking conditions. Fig. 3 highlights the complexity. The latter stage of the project is directed at exploring the upscaling of the laboratory dynamical processes to full-scale oceanic conditions under high wind and hurricane forcing.

The turbulence simulation method uses a novel approach that allows coupling turbulent winds to an underlying three-dimensional time-dependent wave field. In the simulations, the surface wave fields, which contain the essential breaking dynamics, are externally prescribed, i.e., space-time wave field measurements are imposed as a lower boundary condition in the computations. The LES code is highly parallelized and all the computations are performed on parallel supercomputers.

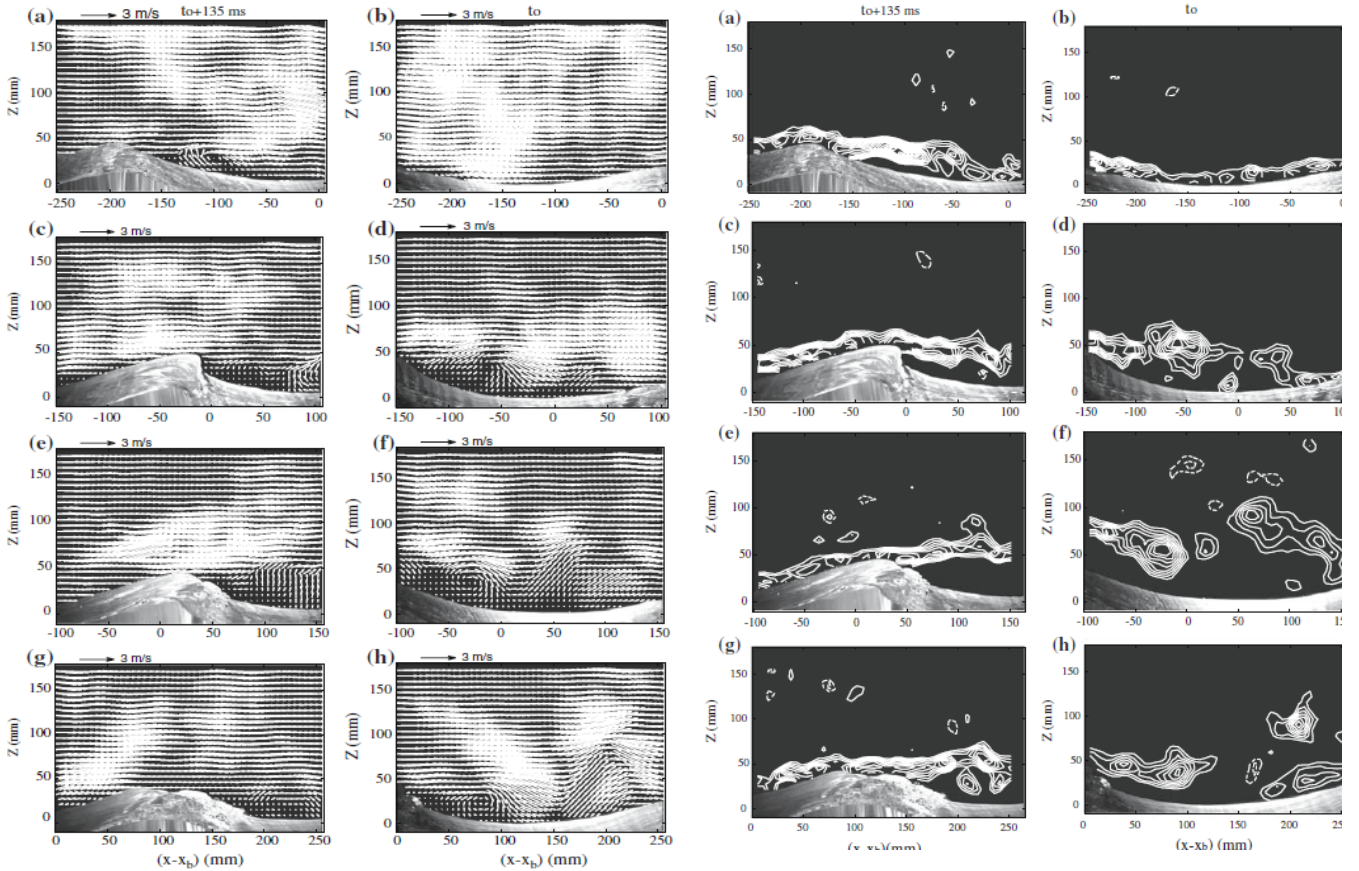


Figure 3. Instantaneous velocity fields in the laboratory frame measured over four distinct waves at various stages of the breaking process. In the left group of 8 panels, each left image (a, c, e & g) represents the flow field over a wave measured 135 ms after the one seen in the right images (b, d, f & h). In (a, b) the wave is not breaking (fetch $x_b = 4.70$ m), (c, d) the wave is at incipient breaking ($x_b = 4.6$ m), (e, f) the wave is fully breaking ($x_b = 4.55$ m), (g, h) the wave is at the end of the breaking process ($x_b = 4.45$ m). The right group of 8 panels show the matching instantaneous vorticity fields corresponding to the images shown in the left 8 panels. These are figures 8 & 9 from Reul et al. (2008).

WORK COMPLETED

Our initial approach concentrated on how closely the LES modeling framework developed by Sullivan (2010a) can replicate the findings reported in the laboratory investigation of Banner (1990), which studied the marginal effect of breaking on the airflow over very young, strongly forced propagating wind waves. The reference wind speed (U_{ref}) to wave speed (c) ratio was ~ 10 , with $c/u_* \sim 1$, where u_* is the wind friction velocity. Consistent with many other studies, U_{ref} was taken here to be the mean wind speed at the height of one-half of the wavelength above the mean water level. In summary, Banner (1990) sought to isolate and quantify breaking-induced separated air flow effects through detailed pressure and velocity measurements of the aerodynamic wave form drag and total drag, comparing breaking wind waves and comparably steep unbroken wind waves. It was found that the local waveform drag nearly *doubled* over the breaking waves - a very strong effect. Further, the average waveform drag contributed about 70-75% of the total wind stress on the water surface for both maximally steep unbroken (incipient breaking) and strongly breaking wave cases, and these total wind stress levels also nearly *doubled* for the breaking waves (as seen in Fig. 1(a)).

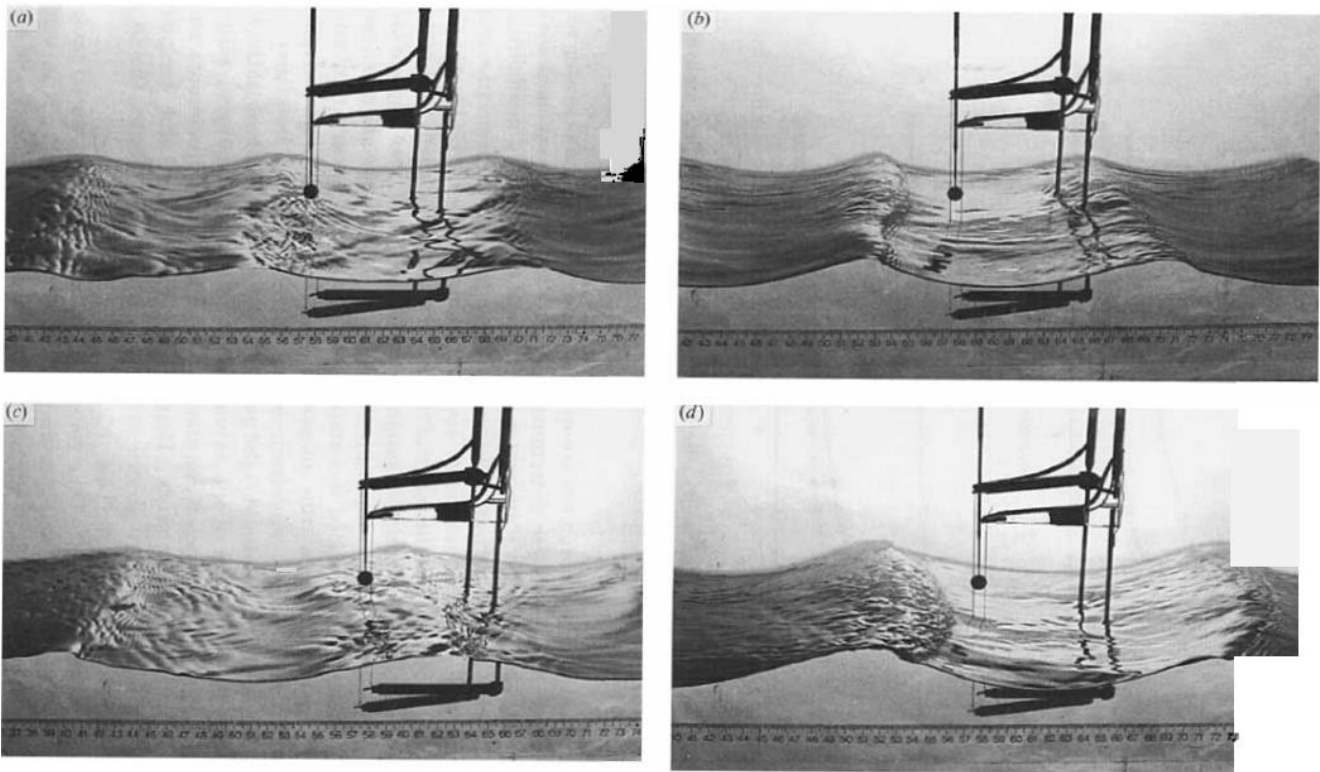


Figure 4. Typical paddle-initiated, wind-forced breaking and incipient breaking waves. The scale is in cm. The wind speed was 5.5 m/s from left to right. (a) 3.35 Hz incipient breaking waves (b) 3.35 Hz breaking waves (c) 2.85 Hz incipient breaking waves (d) 2.85 Hz breaking waves.

We developed initial representative wave elevation distributions, constructed by digitizing the images in Fig. 4. Initial estimates were made of the fluid surface speed distribution along these profiles by assuming a suitably-scaled cosine distribution for the steep unbroken wave, with a similar distribution for the breaking wave but with a compact downslope velocity distribution starting at the crest and finishing at the leading edge of the spilling breaker. Effects of adding a modulated surface wind drift with a mean value of $0.03U_{\text{ref}}$ (where U_{ref} is the centerline wind speed) were investigated in both cases.

These LES computations were carried out in domains of size $(X_L, Y_L, Z_L)/\lambda$ where λ is the wavelength. The simulations are posed in a channel with periodic sidewalls and are driven by an imposed uniform horizontal pressure gradient. Stress free boundary conditions are imposed at the top of the computational flow domain and thus the total momentum flux varies linearly in z over the height of the channel. A bulk momentum integral over the computational domain defines the total stress balancing the imposed pressure gradient, $\rho u_*^2 = \lambda dp/dx$. Note that the computational problem posing is similar to, but different from the experimental setup, where a growing boundary layer develops in the stream-wise direction (the flow is inhomogeneous in x) and the horizontal pressure gradient in the wind tunnel walls is adjusted approximately so that the stream-wise pressure gradient is nearly zero. The discretization in the computations is (N_x, N_y, N_z) grid points with uniform spacing in the $(x-y)$ directions and a smoothly varying stretched grid in the vertical. The LES is carried out at high Reynolds number and assumes a smooth water surface with an initial surface roughness z_0/λ . Calculations were run until a statistically steady state is reached, in about 30-50 large-scale turnover times. For the results, wind and pressure fields are made dimensionless by $(u_*, \rho u_*^2)$ and all lengths are made dimensionless by λ , where ρ and u_* are, respectively, the air density and wind friction velocity.

Initial LES snapshots of the horizontal wind field in an $x-z$ plane for a case with incipient breaking (left panel) and active breaking (right panel) are shown in Fig. 5. The wavelength λ was 0.233 m for the incipient breaking case and 0.235 m for the active breaking case. The corresponding wave heights were 0.178 m and 0.240 m respectively. It is evident that the flow remains attached to the wavy surface in the left panel, while there is significant flow separation at the surface in the right panel. Hence the LES captures the strong difference that the breaking imparts, just as observed by Banner (1990). We investigated the total aerodynamic drag and the form drag predicted by the simulation model. Initial estimates indicated that the drag for the incipient case was too low, so we systematically investigated model sensitivity to the surface velocity and choice of initial roughness length.

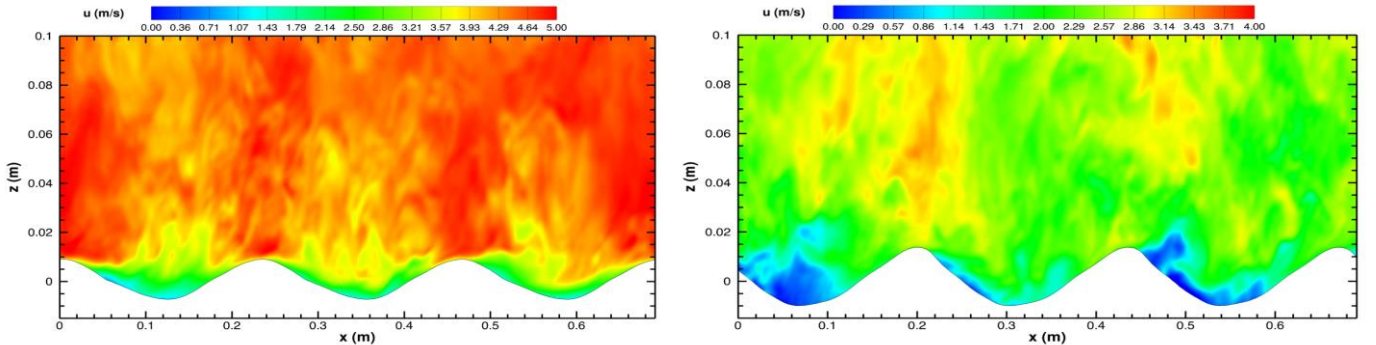


Figure 5. LES snapshots of the horizontal wind field in an $x-z$ plane for a case with incipient breaking (left panel) and active breaking (right panel). Wind and waves travel from left to right. Note the consistent separated flow regions (blue) along the surface for the actively breaking case (right panel), which are absent in the incipient breaking case. This has a very strong effect on phase-shifting the surface pressure field along the wave profile, amplifying the form drag and total drag on the water surface.

Our effort continued on refining how closely the LES modeling framework developed by Sullivan could replicate the findings in Banner (1990); where the average waveform drag contributed about 70-75% of the total wind stress on the water surface for both unbroken and breaking wave cases, with the total wind stress levels also nearly doubling when the waves were breaking.

RESULTS

The following Figures 6 to 9 illustrate: the incipient and breaker wave profiles and the differences in the wave-induced pressure field; the near-surface wind speed over the wave field highlighting the extent of reverse flow (separation) zones; the mean vertical wind field structure showing flow separation zones; and the associated mean velocity profiles in comparison with observations.

In Fig. 6, we note that both the low pressure values over the crest and the high pressure levels on the windward face are reduced for the breaker case, but the phase shift between the high pressure and the wave trough is larger. This results in an enhanced wave form drag given by the pressure-waveslope correlation $\langle p\zeta_x \rangle$, where $z=\zeta(x,y,t)$ is the wave surface elevation. A discussion of the correspondence between computed and measured wave form drag is given below.

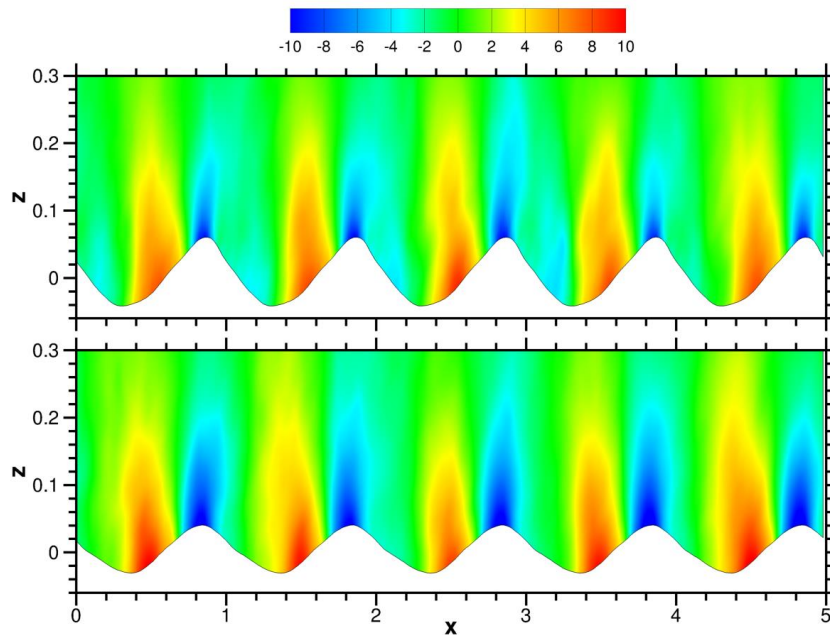


Figure 6. Vertical x - z slice of phase-averaged pressure perturbations $p/\rho u_*^2$ from averaging the pressure in the y direction and plotting the contours (ρ is the air density). Wind and waves travel from left to right. Upper panel is the breaker case and the lower panel is the incipient case. This figure also shows the difference in wave profile shape between the two cases. The color bar is the same for the two panels.

Kinematic details

Representative details of the wind field associated with the pressure fields in Fig. 6 above are shown in Figs. 7-9 below. Here, Figs. 7 and 8 provide a visual impression of difference in the flow fields over the two wave surface conditions, active breaking and incipient breaking. The active breaker has much stronger flow separation on the average, which results in enhanced form drag as described above. This effect also modifies the mean wind velocity profile, as shown in Fig. 9.

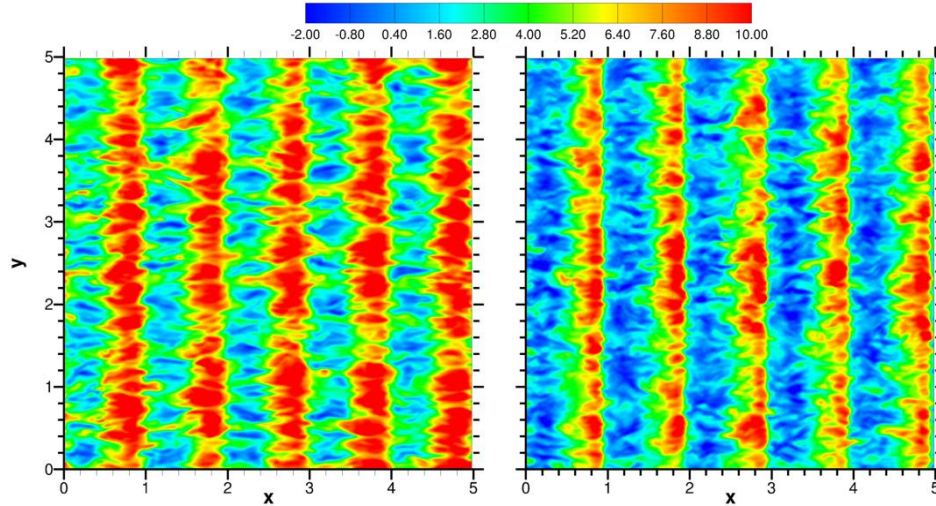


Figure 7. This figure shows an x - y slice (plan view) of the horizontal u field close ($z/\lambda = 0.0163$) to the water surface, where λ is the water wave length. The color bar is the same for the two panels. Left panel is the incipient case and right panel is the breaker case. It is seen that the incipient case has only small pockets of $u < 0$ (dark blue) whereas in the strong breaking case, these regions of reverse flow exist over much of the span-wise extent. The waves are 2D but the wind fields are turbulent and 3D.

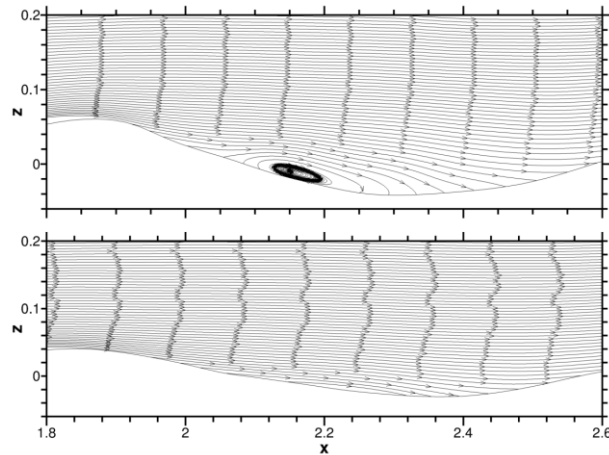


Figure 8. Vertical x - z slice showing streamlines generated from the phase-averaged (u, w) wind components. This was computed for an arbitrary x location in the domain over a one wavelength extent. The active breaker case (upper panel) shows a strong recirculating separation zone. The incipient case (lower panel) shows a far weaker mean recirculation near the trough.

Sensitivity to wave surface conditions

The active breakers, being 30% steeper, have much stronger flow separation on average, which results in enhanced form drag as described above. This effect also modifies the mean wind velocity profile, as seen in Fig. 9. The effect of adding a wind drift layer has been calculated and is shown in this figure. The wind drift is seen to decrease the wind speed relative to the water surface, which decreases the surface stress. The correspondence with the observations of Banner (1990) is encouraging, especially given the difference due to the way the LES problem is posed and the different averaging used in the calculated and observed profiles, as described in the caption.

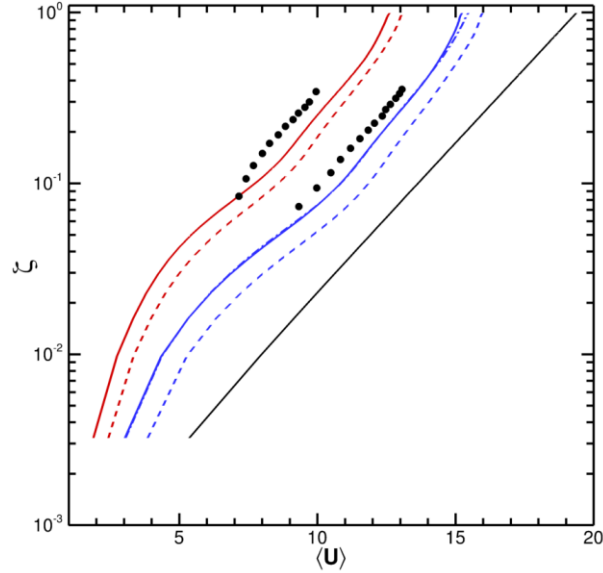


Figure 9. Comparison of our LES mean wind velocity profiles with observed (Banner, 1990). The LES profiles are referenced to the local surface elevation $\zeta=0$, while the measured profiles are from the mean water level $z=0$. The incipient cases are in blue, active breaker cases are in red, dashed lines have wind drift added, and solid lines have no wind drift. The black points are measured profiles from Banner (1990). The black straight line is the familiar wall layer log law for solid flat boundaries, where a roughness length with $z_o = 1.0 \times 10^{-4}/\lambda$ has been used. Note that wind speeds are normalized by u_* and lengths by their respective wavelengths (λ).

It is evident that the flow generally remains more strongly attached to the wavy surface for the incipient case than the breaker case, which shows more widespread and stronger separation effects. Hence the LES was able to capture the strong difference that the breaking imparts, as observed by Banner (1990). We compared the total aerodynamic drag and the form drag predicted by the model, and investigated model sensitivity to surface steepness, surface velocity, initial roughness length and surface profile steadiness. Preliminary results with an initial z_o twice the original level provided a much closer match to the observed wind profiles. Also, increasing the initial z_o resulted in an enhanced form drag, as did increasing the slope of the incipient breaker. The drag estimates were difficult to compare directly due to the way the LES computation had to be set up, but we did manage to systematically investigate how closely the LES model implementation could capture the physics of the laboratory experiment by varying the control parameters. We also noted that departure from steady waveforms should also be investigated.

Model resolution sensitivity

We further refined our LES simulations regarding sensitivity to the grid mesh resolution. In previous work, it was noted that some LES statistics, in particular high-order moments, were sensitive to the grid mesh resolution for boundary-layer flows with flat lower boundaries (e.g. Sullivan and Patton, 2011). Thus, the calculations were repeated using (512 x 512 x 128) grid points compared to the previous computations using a mesh of (256 x 256 x 128); the domain size ($X_L; Y_L; Z_L$)=(5; 5; 1) was held constant. We refer to these LES as fine and coarse grid solutions, respectively. The fine grid computations used four times as many grid points, but required 8 times more computational resources to achieve the same number of large eddy turnover times (~ 50) owing to the reduction in the timestep on the fine grid. We found the fine mesh runs were similar in character to the coarse mesh runs, but were in closer agreement with the observed wind profiles. Our analysis of the LES solutions also

included computation of numerous statistics, extensive flow visualization and movies of the solution fields.

Further results from our fine mesh simulations over steady incipient and active breakers are shown in Figs. 10-14. The visualization in Fig. 10 shows contours of spanwise vorticity $\omega_y = \partial u/\partial z - \partial w/\partial x$ for turbulent flow over an incipient breaker. Here we visualize vorticity, since it is Galilean invariant, i.e., it is independent of the wave phase speed c , and thus is one of the useful metrics for gauging the presence of flow separation over a moving boundary. The visualization shows an intense concentration of vorticity on the forward face of the wave that is compacted into a shallow layer at the wave surface. Animations further show that this vorticity layer intermittently detaches from the wave surface near the wave crest and then often oscillates vertically above the wave trough as it is advected downstream. The vorticity layer serves to isolate slow moving fluid in the wave trough from the faster moving overlying turbulent flow. The left panel of Fig. 10 shows that the vorticity layer near the surface and also in the separated flow region contains strong vortical cores; these vortices are identified using the well-tested and documented technique described by Zhou et al. (1999) and Adrian (2007). In this image notice how the vortical cores leave the wave surface in the separated regions and propagate into the outer turbulent flow. Overall, these results support the premise that turbulent flow separation occurs over incipient and active breakers in agreement with the observations by Veron et al. (2007).

In our LES the net form (or pressure) drag D is the spatial integral of the pressure-waveslope correlation; in the LES-transformed coordinates $(x, y, z) \Rightarrow (\xi, \eta, \zeta)$

$$D = \iint \frac{P}{J} \zeta_x d\xi d\eta$$

where J is the Jacobian of the grid transformation between physical and computational space and ζ_x/J is essentially the waveslope. Fig. 11 shows the spatial distribution of the pressure-waveslope

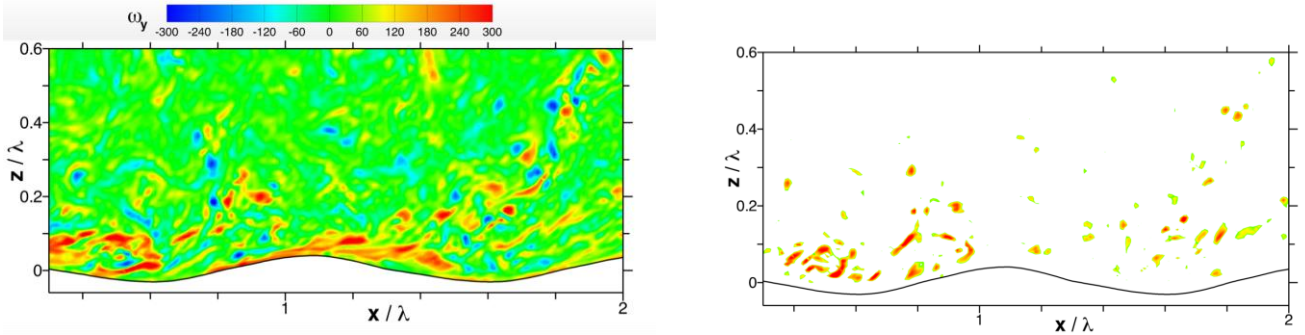


Figure 10. Snapshot of instantaneous spanwise vorticity ω_y contours in an x - z plane (left panel) from LES over incipient breakers using a fine mesh of $(512 \times 512 \times 128)$ gridpoints. Wind and waves travel from left to right. The vorticity is normalized by λ/u_* . Notice that a vigorous (positive-signed) vorticity layer remains attached to the forward face of the wave, but separates from the wavy surface beyond the wave crest and propagates into the overlying turbulent flow. The right panel shows that this vorticity layer contains strong vortices. Here the vortical cores are identified by the complex eigenvalues of the velocity gradient matrix $\partial u_i/\partial x_j$, i.e., the so-called “ λ_{ci} method” of Zhou et al. (1999). The vorticity layer leaving the crest of the wave is suggestive of flow separation as observed by Veron et al. (2007) in a wind-wave tank.

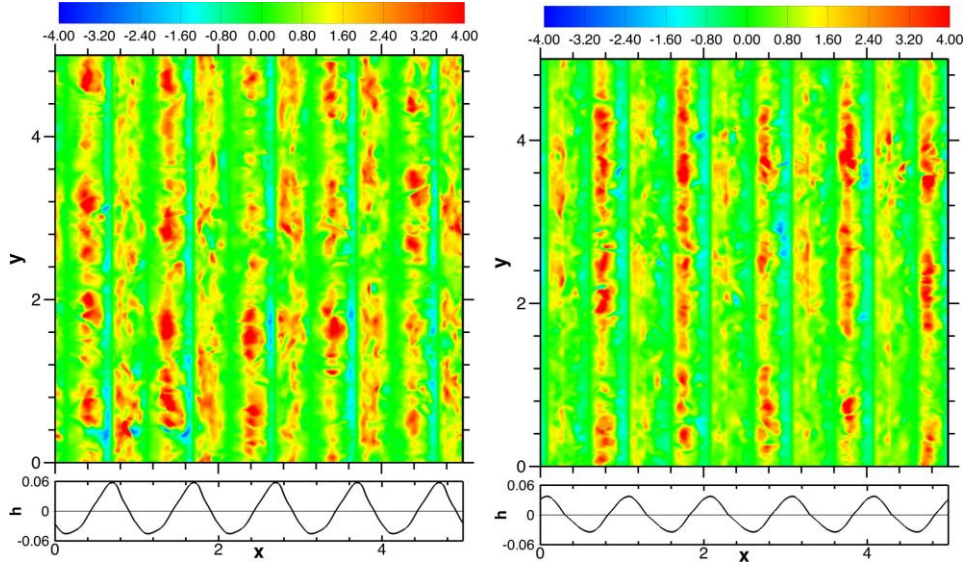


Figure 11. Instantaneous contours of pressure-waveslope correlation (or form drag) $p\hat{h}/\partial x$ in an x - y plane for active (left panel) and incipient (right panel) breaking. For reference, the two-dimensional wave height $h(x, t)$ is shown in the bottom of each panel. Pressure is normalized by ρu_*^2 (ρ is the air density), and the winds and waves both propagate from left to right. Notice a large fraction of the total form drag occurs on the windward face of the waveform, i.e., where positive pressure is well correlated with positive wave slope. The flow separates near an upstream wave crest and stagnates (re-attaches) on the windward face of a downstream wave generating high positive pressure. The form drag is (74, 54)% of the total drag for (active, incipient) breaking, respectively. The red contours are regions where the local pressure drag is more than 5 times the mean value obtained by averaging over the entire domain.

correlation for active and incipient breakers. Key features to notice are: $p\zeta_x/J$ is spatially intermittent and varies considerably with the spanwise y -coordinate despite the two-dimensional character of the underlying imposed waves. Closer inspection of Fig. 11 also shows that the largest values of pressure-wave slope correlation frequently occur on the forward face of the wave, i.e., where positive pressure is well correlated with positive wave slope. This result can be understood by noting that the vorticity layer in Fig. 10 separates near the wave crest but often stagnates (re-attaches) on the forward face of the downstream wave generating high local positive pressure. There are also significant contributions to the total drag from regions just forward of the wave crest where negative pressure is well-correlated with negative wave slope. The local value of the pressure-waveslope correlation (the red regions in Fig. 11) often exceed the mean value by more than a factor of 5.

Averaged wind profiles from the computations are compared with the observations by Banner (1990) in Fig. 12. We find (very) good agreement between the observations and the fine mesh LES solutions. In this comparison, the LES winds are averaged over ζ and η at constant values of the wave-following coordinate ζ whereas the observations are collected at a fixed height above the mean water level. In the LES the constant ζ surfaces become nearly level surfaces at the vertical location where the observations are collected. Sullivan et al. (2014) shows that averaging in wave-following coordinates is advantageous as it allows computation of the winds, and also the fluxes, down to the water surface, i.e., below the wave crests. We speculate that the improved simulation-observation agreement is a consequence of better resolution of the separation and re-attachment points and reduced reliance on the subgrid-scale model. At constant ζ/λ the leftward shift of the wind profile with active breaking compared to the incipient case implies a greatly increased surface roughness z_o .

Models of the wave-induced boundary layer typically adopt a constant flux assumption near the water surface and then seek to partition the momentum flux into turbulent and wave-induced pieces as function of height in the constant-flux layer. These ideas can be evaluated using our LES results for flow over active and incipient breakers. The steady ensemble-average streamwise momentum balance equation in our LES assuming periodic sidewalls reads (Sullivan et al., 2014).

$$\left\langle \frac{P_x}{J} \right\rangle = -\frac{\partial}{\partial \zeta} \left\langle \frac{P}{J} \zeta_x + u(W - z_t) + \frac{\tau_{1k}}{J} \zeta_{x_k} \right\rangle \quad (\text{eq. 1})$$

where the large-scale driving pressure gradient P_x is balanced by the vertical divergence of three terms, viz., in left-to-right order, pressure, resolved turbulence and subgrid-scale (or viscous) terms. In the above expression, W is the contravariant flux velocity in the vertical direction normal to a $\zeta - \eta$ surface, z_t is the grid speed of each point in the computational mesh, and $\langle . \rangle$ denotes a horizontal average. In our problem the lower boundary condition is $W = z_t$ at $\zeta = 0$ so that there is no flow across the wavy surface. Fig. 13 shows the vertical distribution of the streamwise momentum flux components contributing to the right-hand-side of (eq. 1) for active and incipient breakers. First, the total flux varies almost linearly over the height of the computational domain and accurately satisfies global momentum balance. However, when the fluxes on the right-hand-side of (1) are plotted on a logarithmic vertical axis as in Fig. 13 we find a shallow constant flux layer near the water surface extending up to about $\zeta/\lambda \sim 0.06$. It is interesting to notice that this is approximately the maximum crest height as shown in the bottom panel of Fig. 11. In computations of a full marine boundary layer with height $z_i \sim 500$ m (Sullivan et al., 2014), it was found that the constant flux layer is deeper, extending up to more than $0.1\zeta/z_i$. In the present calculations, the pressure-waveslope correlation, turbulent flux and subgrid-scale terms all vary smoothly with height above the wave surface, and it is apparent that in the case with active breaking, the pressure drag dominates the flux at the water surface, carrying almost 75% of the total wind stress.

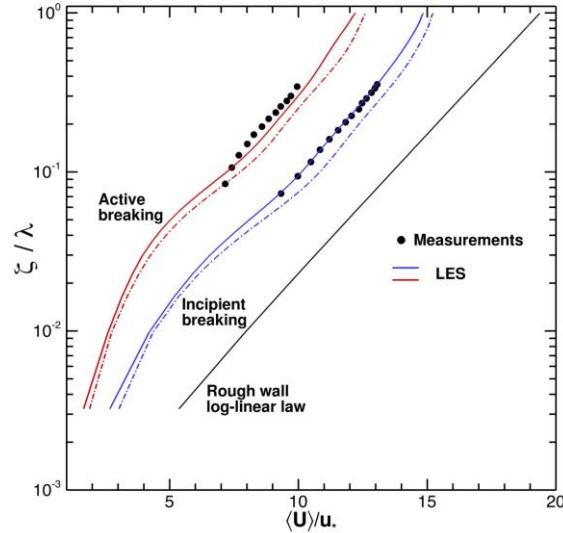


Figure 12. Influence of model resolution on the vertical profile of average streamwise wind $\langle U \rangle$ normalized by surface friction velocity u_* for incipient (blue lines) and active breakers (red lines) from LES. Solid and dash-dot lines use grid meshes of $(512 \times 512 \times 128)$ and $(256 \times 256 \times 128)$ grid points, respectively. A reference rough surface log-linear wind profile for no resolved surface waves is also shown by a solid black line. The vertical offset of the wind profile at constant $\langle U \rangle/u_*$ reflects the increased roughness induced by breaking waves. Spatial averaging in the LES is carried out in wave-following coordinates at constant ζ values. Solid bullets are mean wind speed measurements made at fixed heights above the mean water surface in Banner (1990).

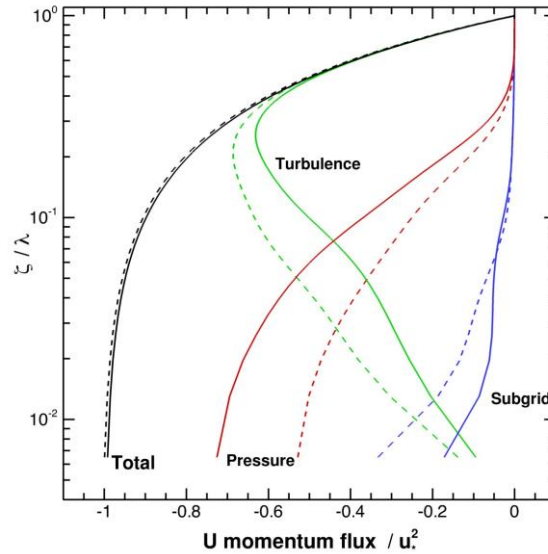


Figure 13. Vertical profiles of the terms in the ensemble average streamwise momentum budget computed in the LES wave-following coordinates (Sullivan et al., 2014). Flow over incipient and active breakers is indicated by dashed and solid lines, respectively. The contributions to the streamwise momentum are: pressure-waveslope correlation (form drag) $p\zeta_x/J$ (red curves), vertical turbulent momentum flux $u(W-z_t)$ (green curves), the subgrid-scale flux (blue curves) and their sum, the total flux (black curves). Fluxes are normalized by the total stress u_*^2 and results used a fine grid of $(512 \times 512 \times 128)$ points.

Sensitivity to the water surface speed distribution

Classical airflow separation over a rigid surface typically occurs under decelerating flow conditions associated with adverse pressure gradients. The flow at the boundary separates from it, creating a separation streamline originating on the boundary that separates the ejected wall layer fluid on one side and a weak, near-stagnant recirculating flow on the other side. It was argued by Banner and Melville (1976) that this physical picture for a wavy water surface has a possibly analogous behavior, but only if the wave is about to break or is breaking. The breaking crest region provides the only scenario where a stagnation point exists on the boundary, relative to the translating wave surface, for a separation streamline to develop from the boundary. Subsequent studies have confirmed the occurrence of separation over breaking waves (e.g. Reul et al., 2008). Banner (1990) was undertaken to investigate whether wave breaking leads to a significant increment in waveform and total drag. The underlying question is whether the separation is associated primarily with the steep wave geometry, or with the breaking. Thus as part of the present study, we ran a comparative simulation using the same steady geometrical waveform (‘active breaker’), but added a simulated wind drift layer. This was simulated by superimposing on the surface orbital velocity distribution a modulated cosine surface layer current in phase with the wave crest with a mean strength of $0.03 U_{10}$ based on published observations. Here U_{10} is the wind speed extrapolated to 10 m above the mean water level based on a log-layer mean velocity profile. We investigated sensitivity of the form drag, tangential stress and mean wind velocity profile to changes in the surface kinematical conditions. The results are summarized in Fig. 14 below.

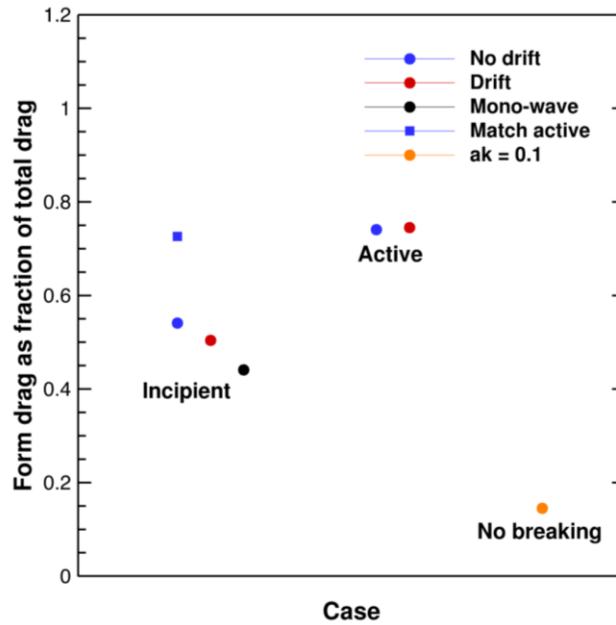


Figure 14. Sensitivity of the form drag to total drag ratio to wave steepness and surface drift velocity. Note that when the steepness of the incipient waves is increased to match the active breaking waves, the form drag fraction now coincides. Also, the effect of wind drift current is seen to be secondary.

These steady shape simulations reveal that the ratio of form drag to total drag is dependent primarily on the wave form geometry, in particular the wave steepness. Also, the sensitivity to surface velocity is seen to be secondary. This is seen in the slight increase in near-surface mean velocity profiles and corresponds to a slight reduction in the wave form drag in the above two figures (Fig. 9 & Fig. 14).

Sensitivity to the initial roughness length

The simulations reveal that when the initial z_o is increased, the mean velocity profiles show increased slowdown near the water surface. Also, we investigated the sensitivity of the incipient breaker results to increasing its steepness by 15% additional to the increased z_o , and further reduction is seen in the near-surface wind profile.

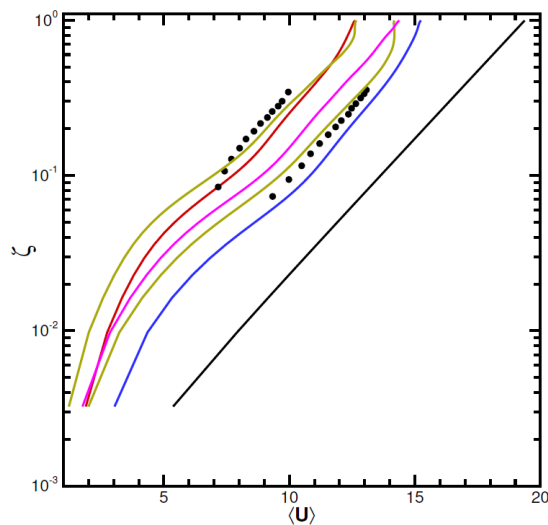


Figure 15. Impact of initial roughness length on mean velocity profiles. Two cases with a larger initial z_o and one case where the incipient breaker slope was increased by 15% and with enhanced initial z_o . Shown are the wind profiles for the different runs without drift. 1) blue line: incipient breaker, $z_o=1.0 \text{ e-}04 \text{ m}$; 2) red line: active breaker, $z_o=1.0 \text{ e-}04 \text{ m}$; 3) faded green: case 1) & 2) $z_o=2.0 \text{ e-}04 \text{ m}$; 4) pink line: incipient breaker with 15% larger steepness AK and $z_o=2.0 \text{ e-}04 \text{ m}$.

Correspondingly, form drag levels are enhanced with the increased z_0 . With the larger initial z_0 , the active breaker case has a form drag/wind stress ratio of $\sim 70\%$ and the incipient breaker case $\sim 50\%$. The pink case shows the sensitivity of the form drag, additional to the increased initial z_0 , to increasing the steepness of the incipient breaker by 15%, which is seen to further enhance the form drag.

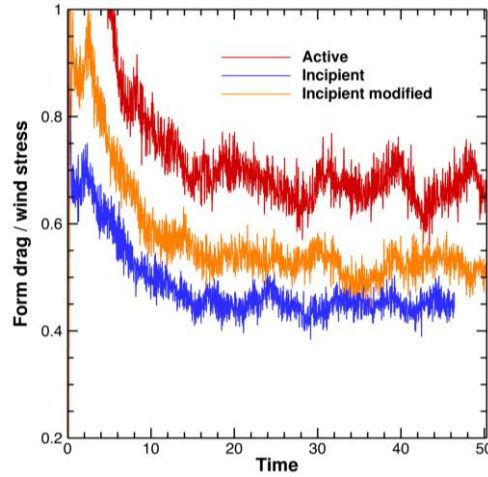


Figure 16. Times series of form drag as a fraction of total wind stress. Behavior for $t < 15$ is the start-up transient where the turbulence is not fully developed. A time average from $30 < t < 50$, during which the turbulence fluctuates would provide a stable average. Red is the active breaker, blue is the incipient, orange is the incipient but with its amplitude increased by 15%. Increasing the incipient case to larger steepness increases the ratio towards the active breaker case. The runs in this plot use the coarser mesh of $256 \times 256 \times 128$.

Effects of increasing wave age at constant wave steepness.

The original wave shapes adapted from Banner (1990) had wave age $c/u^* = (1.58, 1.23)$ based on the published phase speeds and u^* levels. The wave age based on c/U_{ref} was about 0.1, or the driving wind was about ten times the wave speed, indicating that these were very young wind waves. To investigate how the wind-wave coupling mechanisms change as the wave speed moves towards the wind speed, further LES cases were run, assuming that the non-dimensional wave shape stayed the same. The non-dimensional wave age was increased by factors of 5 and 10, which increases the length scales by factors of 25 and 100. The initial z_0 was increased by the same amount so that z_0/λ remained the same as the phase speed was increased. Since the LES code runs in non-dimensional units, the real change was faster wave propagation down the channel and the correspondingly increased orbital velocity at the wave surface.

Our results below show that for this steep wave scenario, even the pressure (form) drag over our model active breaker appears to be strong function of wave age. Similar to the case for simple monochromatic waves of low wave slope (Sullivan et al., 2000), as the wave age increases, the flow separation tends to disappear. The results obtained over a steep ocean wave that is moving fast, i.e. has a larger wave age, bear on whether flow separation is operative. This LES simulation suggests the surface wind flow does not separate even for this very steep wave profile.

Fig. 17 below shows two panels showing the y-averaged vertical velocity $[w(x,z)]$ distribution for the incipient case for two wave ages. The left panel is for very young conditions simulating the incipient case in Banner (1990), where the wave age $c/u^* \sim 1.58$. This case shows intermittent separation as stagnant zones adjacent to the surface downwind of the crests. The right panel is the same wave

geometry but now the wave age $c/u^* \sim 7.9$. The elevated w maxima now present above the wave crests are signatures of a critical layer, as shown in Sullivan et al. (2000). Thus increasing the wave age for the same shape wave causes a flow transition from a separated regime to a non-separated regime with a critical layer.

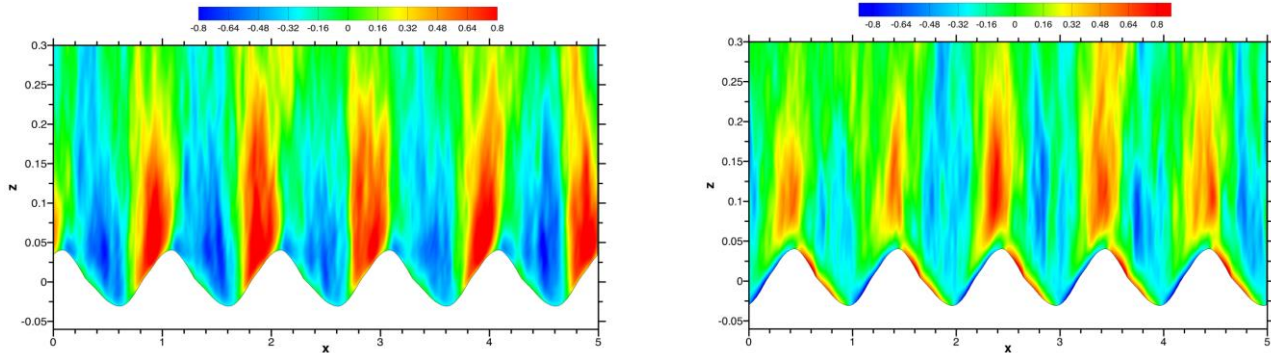


Figure 17. Vertical velocity $[w(x,z)]$ distributions for the incipient breaker wave shape in Banner (1990) for two wave ages. The left panel is for very young conditions where the wave age $c/u^* \sim 1.58$. This case shows intermittent separation as stagnant zones adjacent to the wave surface downwind of the crests. The right panel has wave age $c/u^* \sim 7.9$.

The effect of increasing the wave age also translates to the case with the active breaker, where Fig. 18 shows plots of phase averaged streamwise velocity (normalized by u_*) for the active breaker case. The left panel simulation matches the Banner (1990) tank measurements with $c/u^* \sim 1.2$, while the right panel is the same shape but has $c/u^* \sim 6$. Compared to the tank wavelength of 0.25 m, this wave has a wavelength λ of 5.75 m. The simulation with $c/u^* \sim 1.2$ has persistent airflow separation while the second case has little or none. Note that the color bar changes between the two images. The trend of these findings is consistent with the recent measurements by Buckley and Veron (2016), but for somewhat lower wave steepness conditions.

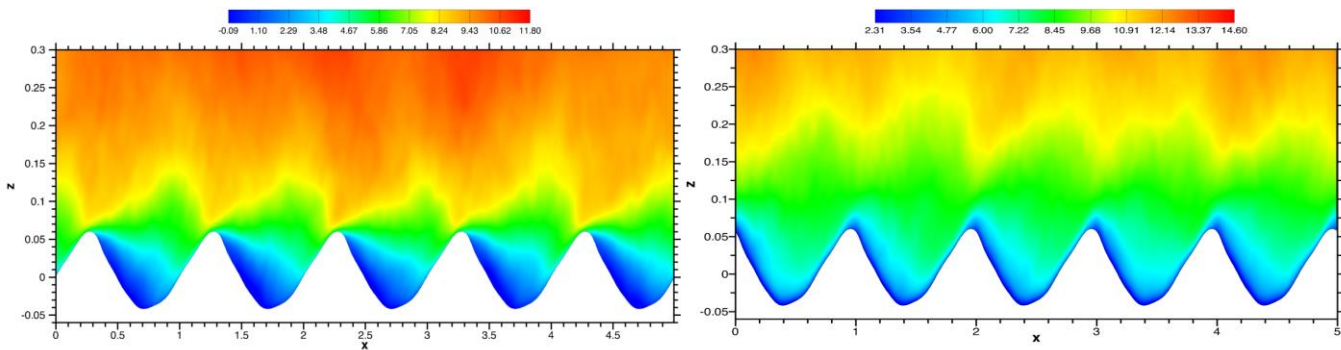


Figure 18. Aerodynamic effect on the phase averaged streamwise velocity (normalized by u_*) of increasing the wave age for the active breaker case. The left panel shows the very young active breaker case with $c/u^* \sim 1.2$, while the right panel is the same shape but has $c/u^* \sim 6$. Noting the change in the color bars, the strong separation seen in the left panel is now absent from the right.

The implications of increasing the wave age on the relative strength of the pressure drag/total stress ratio are seen in the time series plots in Fig. 19 below. Clearly, with increasing wave age, the occurrence of air flow separation decreases, causing a decrease in the form drag relative to the total wind stress. In the right panel, there is no evidence of flow separation for the incipient breaker case when $c/u^* = 15.8$, and the low value of pressure drag is similar to wave-driven wind cases.

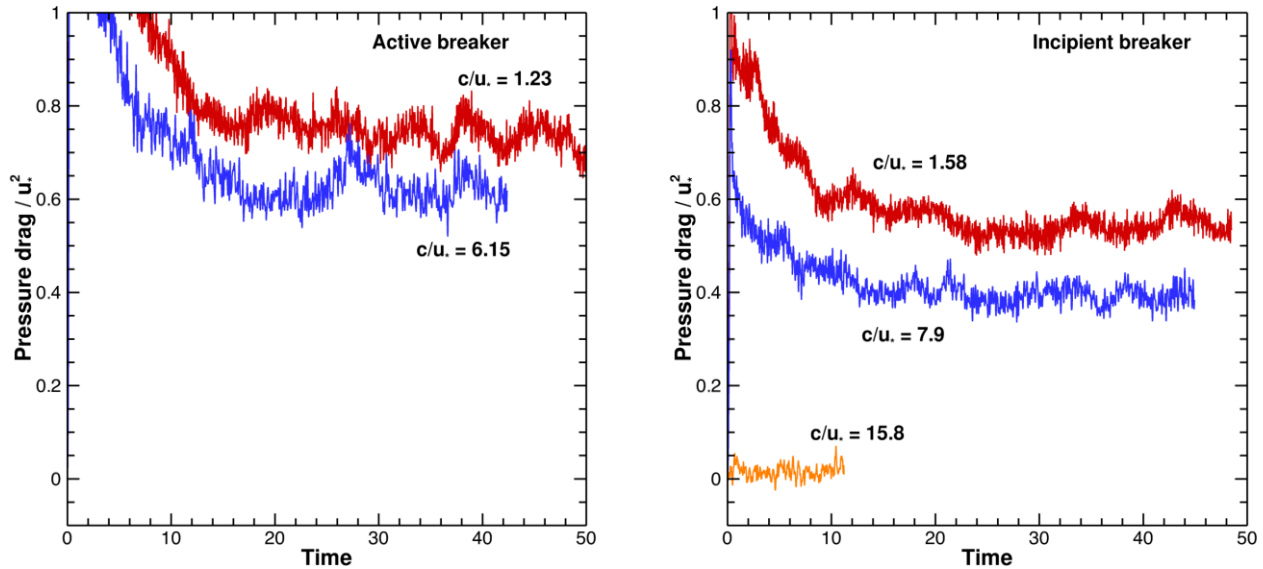


Figure 19. Consequence of increasing the wave age on the relative strength of the pressure drag/total stress ratio for our two steep, fixed waveforms: active and incipient breakers. Shown are time series plots of this stress ratio at the indicated wave ages. The occurrence of air flow separation decreases as the waves age increases, causing a decrease in the form drag relative to the total wind stress. In the right panel, there is no evidence of flow separation for the old incipient breaker when $c/u_* = 15.8$.

Effects of strong modulation on turbulent flow over a train of unsteady steep wave packets

The intermittent nature of the breaking process combined with the unsteady group structure of the underlying surface waves present significant knowledge gaps. In this context, results from several laboratory studies of deep water wave groups have suggested (Rapp and Melville (1990), Stansell and McFarlane, (2002), Jessup and Phadnis (2005)) that breaking-crest speeds are typically O(20%) lower than expected from linear-wave theory, contrary to the expectation from Stokes theory that the steeper class of breaking waves should travel faster than their corresponding linear wave speed. Banner et al. (2014) investigated this numerically and observationally, and identified a remarkable generic behavior for unsteady deep water wave packets in the ocean, namely that as they reach their local maximum height, ALL wave crests travel at a speed about 20% less than the corresponding linear phase speed. The underlying cause is a generic phase-locked secondary leaning motion associated with the unsteadiness and finite spectral bandwidth, as summarized in the figure panels below:

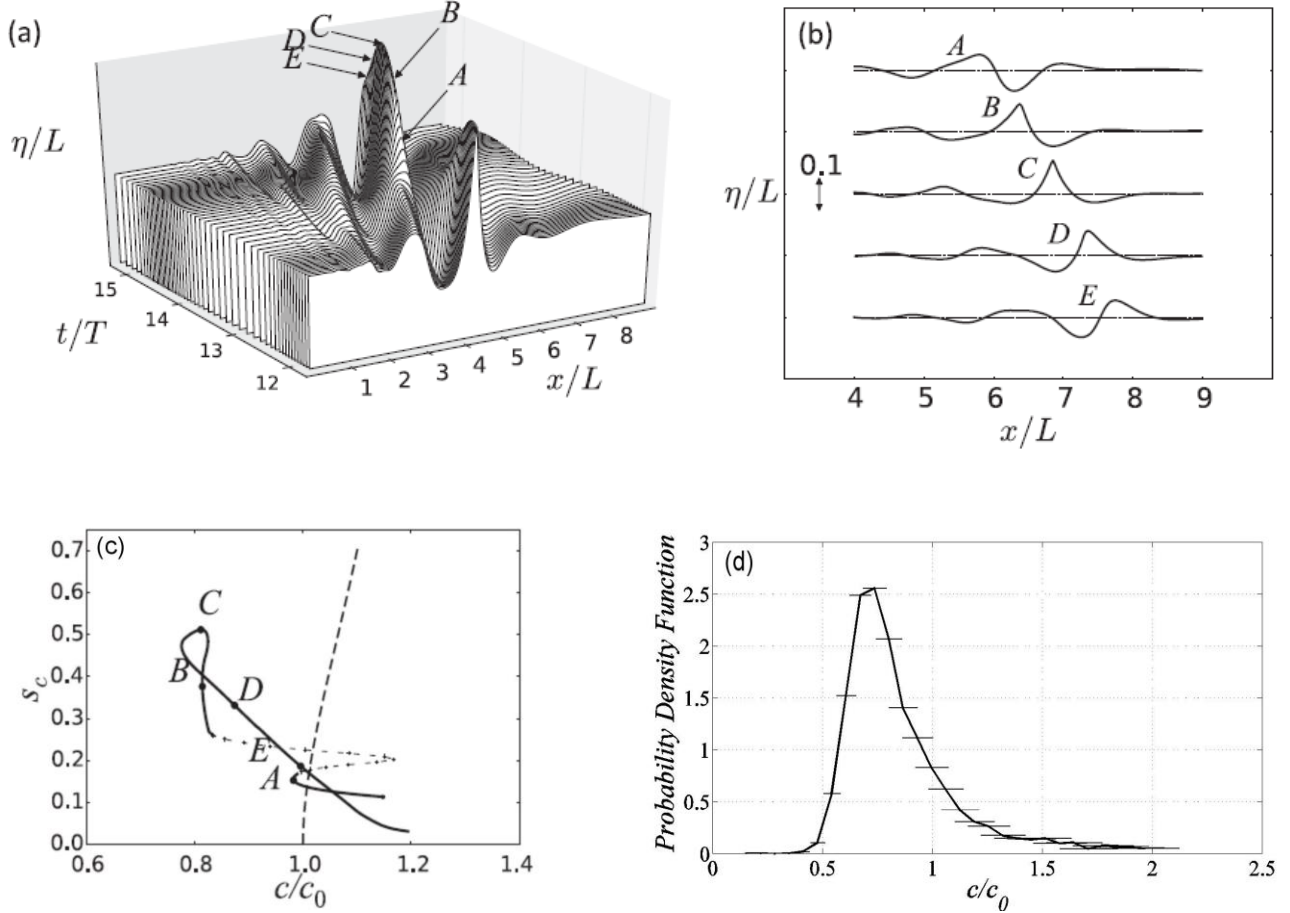


Figure 20. Crest shapes and speeds for the numerically-simulated chirped wave packet shown as a space-time stack in panel (a) with five different evolution times A-E indicated. Panel (b) shows the wave height profile at these times, as the profile transitions from forward-leaning through symmetry to backward-leaning. Panel (c) shows trajectory of the corresponding tallest crest speed c , normalized by c_0 , as a function of the local wave crest steepness S_c (similar to AK, but localized to the crest half-wavelength). Stokes theory prediction is shown (dashed line) for comparison. T and L are reference wave period and wavelength scales characterizing the wave group. Panel (d) shows the probability density function of normalized crest speed c/c_0 (with standard error bars) for all ocean wave crests transitioning through their maximum local steepness. Measurements were obtained from a 35 minute stereo video sequence of very young wind seas forced by Bora winds from an open ocean tower off Venice. The tall peak at $c/c_0 \sim 0.75$ highlights the systematic crest speed slowdown.

With the goal of exploring a new approach to predicting wave breaking onset based on energy flux considerations, we investigated the transition zone between maximally steep waves without breaking and those that proceeded to break, using a large number of nonlinear chirped wave packet evolution simulations. That effort resulted in the discovery of a remarkably simple generic breaking onset threshold that is valid for 2D and 3D breaking in uniform water depths from deep to transitional. While the criterion is based on the energy flux to the steepening crest, the surface signature reduces to a form involving only the ratio of the surface fluid speed u_c to the crest speed C_c . For breaking onset to occur, it was found that this ratio must exceed 0.85 ± 0.01 (Barthelemy et al., 2015).

We extended our LES study to investigate wave forms more representative of natural waves, which occur typically as unsteadily evolving groups. We performed LES using the algorithms described in

(Sullivan et al., 2014), with the steep uniform fixed-profile wave train replaced by a train of unsteady steep wave packets generated by a fully nonlinear wave code (Banner et al., 2014), as described below. For our simulations of realistic steep unsteady wave packets, we adapted the wave packet evolution as shown in top panels of Fig. 20 to synthesize a progression of 3 of these packets that evolve down the fetch of the LES domain, driven by strong wind forcing with $c/u_* \sim 1$. The figures below illustrate typical complex streamline and pressure field behavior, as well as the evolution of the form drag as the train of unsteady packets evolves through the cycle seen in Fig.20(b) above.

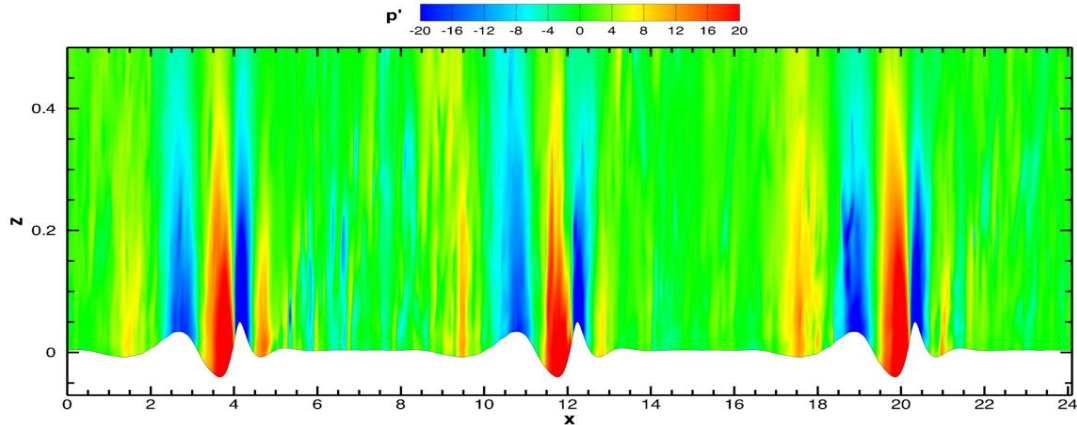


Figure 21. Instantaneous pressure field above the strongly wind-forced unsteady wave packet with $c/u_* \sim 1$. Note the strong penetration of the pressure field into the mean flow above the surface, which increases even further around $T=2$ (see sequence below in Fig. 23)

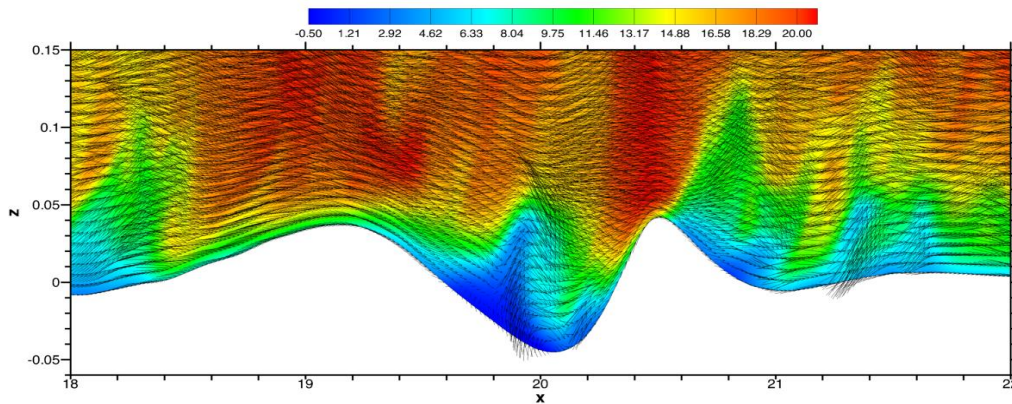


Figure 22. Streamline snapshot showing the transient complex separated flow (dark blue) zones where the fluid velocity reduces to near-zero. Typical pressure fluctuation patterns are seen in Fig. 23 below

In Fig. 23 below we show three snapshots of the normalized fluctuating pressure p'/u_*^2 field for the strongly forced, unsteady chirp packet propagating through the domain as time increases. The maximum drag and largest vertical velocity occur in the middle of the run on the upwind face of the very steep wave, near $T = 2$, accompanying the high vertical extent of the pressure perturbation.

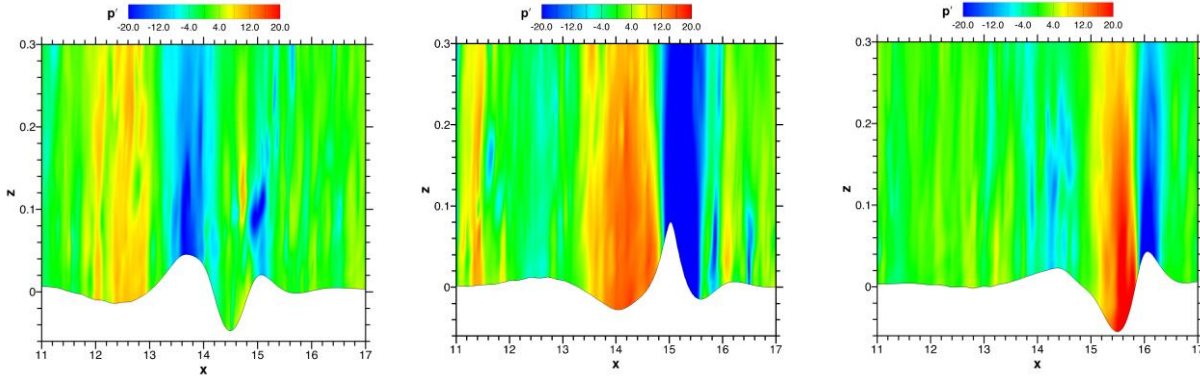
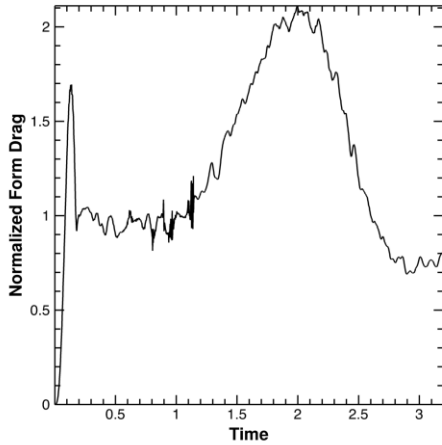


Figure 23. Three snapshots of the normalised fluctuating pressure p'/u_*^2 field for the strongly forced, unsteady chirp packet at times $T=1, 2$ and 3 . Note the large pressure perturbation in the center panel. Changes in the evolving wave packet can be seen as the packet travels through the domain as time increases. The associated changes in the domain-integrated form drag are shown in Fig. 24 below.

Taken over the whole evolution cycle, the wave form drag fluctuates in time, maximizing strongly around $T=2$, as shown in Fig. 24. This corresponds to the large pressure perturbation event around $T=1.9$ (Fig. 24(a)), in synchrony with the largest vertical velocity perturbation (Fig. 24(b)).

(a)



(b)

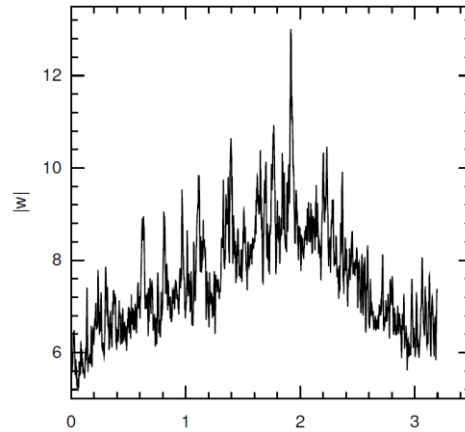


Figure 24. (a) Time series of the integrated pressure (form) drag over all x and y , including the flat sections between the packets, producing the channel average form drag. To highlight the impact of the wave packet unsteadiness, we show a normalization against the initial form drag level at $T=1$. (b) the maximum vertical velocity detected in the channel. This also reaches a maximum around $T = 1.9$, which coincides with the timing of the occurrence of the steep wave event.

To date, we have found that it is not the rms steepness alone that correlates strongly with the form drag, but also the volatility of the steepness. For our unsteady packet, the packet rms slope of the packet at $T=2$ is $O(0.1)$ compared with the steady incipient breaker rms slope of $O(0.25)$, yet both have comparable form drag levels of 0.4-0.5 of the total drag. Further LES simulation runs and analysis are needed to refine understanding of the relative importance of the contribution of unsteadiness to modifying the form drag and total wind stress.

Impact of strong separation on scalar transport

Scalar transport in the presence of separated flows (e.g. over breaking waves) is one of many critical components of air-sea interaction. It is important in numerous applications but can also shed light on wind-wave coupling dynamics. It is often assumed that scalar fluxes are relatively insensitive to the wave state, but this is not necessarily well understood. For example, direct numerical simulation of turbulent flow over waves of small wave slope $AK < 0.1$ highlighted an unexpected wave-induced temperature flux (Sullivan & McWilliams, 2002). As the waves become very steep, air-sea gas transfer is believed to be enhanced by wave breaking, but obtaining direct observational support is very challenging.

To further investigate the mechanics of scalar transport in this study, we added a simple passive (non-interacting) scalar C to our LES model and repeated our simulations of turbulent flow over incipient and active breakers. The boundary conditions on the scalar are a constant uniform value $C_s(x, y) = 1$ at the water surface $\zeta = 0$ and a zero gradient condition $\partial C/\partial z = 0$ at the top of the computational domain. As is customary practice for high Reynolds number flows, the surface scalar flux $C_*(x, y)$ is found by adopting rough-wall relationships between $C_s(x, y)$ and the scalar field at the first model level $C(x, y, \zeta_1)$. We are aware that this surface boundary condition is highly idealized and does not allow for injection of water droplets into the overlying airflow. The scalar simulations are initiated using restart data volumes, with fully developed turbulent fields, archived from past calculations and are run until the turbulence statistics become statistically stationary, approximately 20 large-eddy turnover times $T = h/u_*$, where h is the computational domain height and u_* is the surface friction velocity.

Fig. 25 is an example of a scalar field, specifically the concentration difference $\Delta C = (C_s - C)/C_s$, in an $x - y$ plane at the first model level above the water surface. These are typical snapshots at late time in the simulations and demonstrate clear differences between cases with incipient and active breaking waves. Both images illustrate the spatially intermittent character of the scalar field and also show a strong correlation between the scalar concentration and the underlying wave shape. With incipient

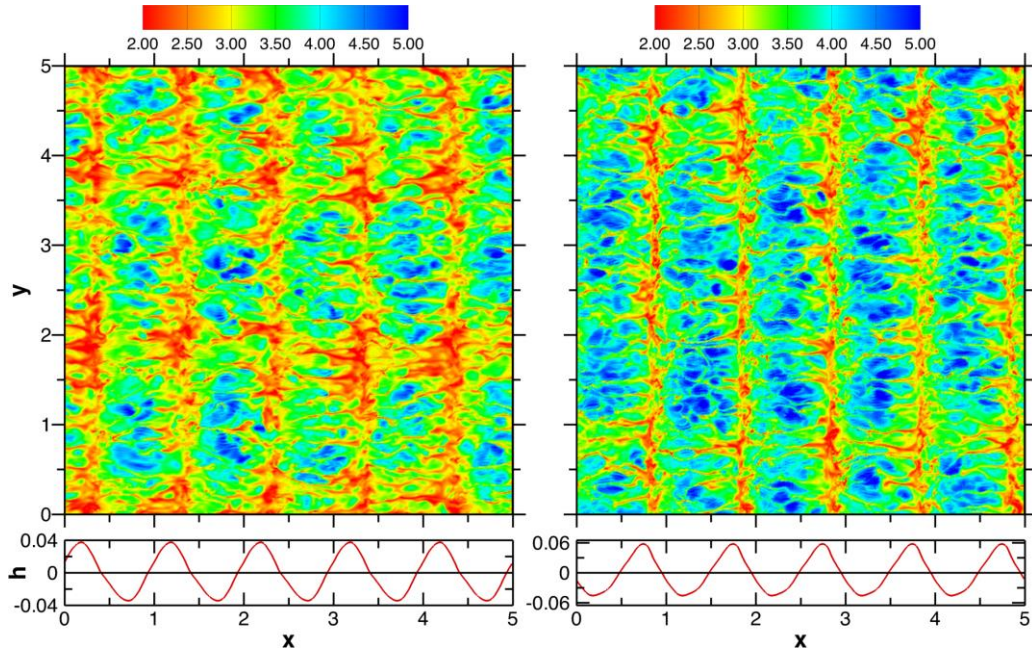


Figure 25. Visualization of scalar concentration difference $\Delta C \times 10^2$ in an $x - y$ plane near the water surface; $\Delta C = (C_s - C)/C_s$ with $C_s = 1$ at the water surface. (Left, right) panels are turbulent flows with (incipient, active) breakers, respectively. The wave height $h(x, t)$ for each flow is shown at the bottom of each panel. Note that high (low) concentrations correspond to red (blue) values of ΔC .

breaking, the scalar concentration is higher than with active breaking and is preferentially distributed spanning a region both aft and forward of the wave crest. In contrast, with active breaking high values of C are concentrated in a narrow y -band just forward of the wave crest, with relatively low concentration over broad regions in the wave troughs. In both simulations, the C field is spatially intermittent even though the wave shape is invariant in y and the surface boundary condition is uniform and constant. The spatial variation of $C(x, y, \zeta_1)$ further implies that the surface scalar flux C_* is also spatially intermittent. Patterns in the scalar fields reflect the advecting velocity fields and in particular, the circulations induced by turbulent flow separation over our steep surface waves. Vertical profiles of average scalar concentration are shown in Fig. 26 for turbulent flow over incipient and active breakers. For reference, we also show the average wind profiles for these two cases as well as the rough wall log-linear relationships for the small parameterized surface roughness applied at the top of the water. As reported previously, the winds slow down markedly in the presence of breaking and then the wind profiles display an upward shift at fixed $\langle U \rangle / u_*$, indicative of an increase in the bulk surface roughness. The simulation results seen in Fig. 26 are in good agreement with the observations by Banner (1990). The impact of breaking on the scalar concentration profiles is somewhat surprising

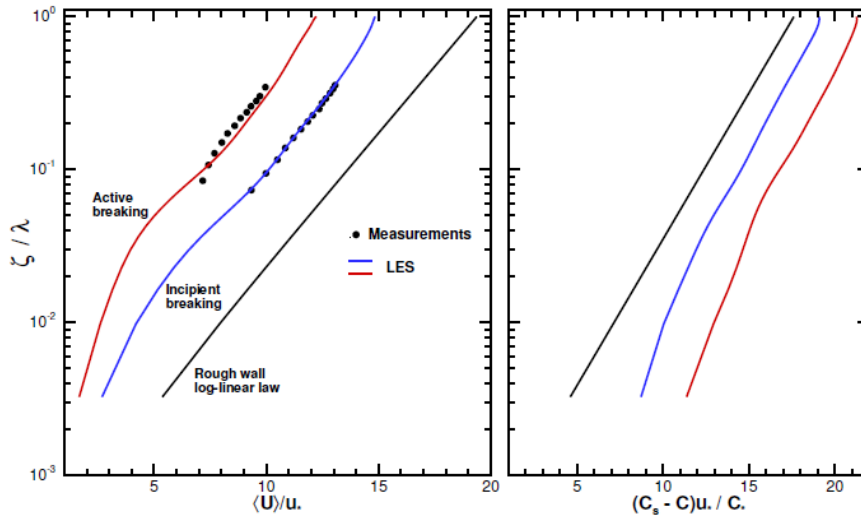


Figure 26. Vertical profiles of average streamwise wind (left panel) and scalar concentration difference (right panel) for incipient (blue lines) and active breakers (red lines) from LES. The LES mesh is $(512 \times 512 \times 128)$ grid points. For reference, rough surface log-linear wind and scalar profiles for no resolved surface waves, $z_o/\lambda = 10^{-4}$, are also shown by a solid black line. The upward vertical offset of the wind profile at constant $\langle U \rangle / u_*$ reflects an increase in the bulk roughness momentum roughness $z_{o,m}$ induced by breaking waves. Solid bullets are measurements of mean wind speed obtained at fixed heights measured from the mean water surface from Banner (1990). However, the downward vertical offset of the scalar profile reflects a decrease in the bulk scalar roughness $z_{o,s}$. The spatial averaging in the LES is carried out in wave-following coordinates at constant ζ .

As expected for a resolved wavy surface, the scalar profiles follow a log-linear relationship above $\zeta/\lambda \sim 0.1$, similar to the wind profiles. However the scalar profiles are shifted downward compared to the rough-wall parameterization, i.e., the impact of steep waves on the scalar profiles is opposite compared to the wind profiles. These results imply that in a bulk sense, the scalars feel a smoother surface. Thus for our laboratory breaking waves, the effective total scalar roughness $z_{o,s}$ decreases while the effective total roughness for momentum $z_{o,m}$ increases. In order to explain this surprising result, we examine the ensemble average equations for streamwise momentum and scalar concentration for turbulent channel flow over moving waves driven by a constant large scale pressure gradient P_x :

$$\frac{\partial}{\partial t} \left\langle \frac{u}{J} \right\rangle = - \left\langle \frac{P_x}{J} \right\rangle - \frac{\partial}{\partial \zeta} \left\langle \frac{p}{J} \frac{\partial \zeta}{\partial x} \right\rangle + u(W - z_t) + \frac{\tau_{1k}}{J} \frac{\partial \zeta}{\partial x_k} \quad (1)$$

$$\frac{\partial}{\partial t} \left\langle \frac{C}{J} \right\rangle = - \frac{\partial}{\partial \zeta} \left\langle C(W - z_t) + \frac{\tau_{ck}}{J} \frac{\partial \zeta}{\partial x_k} \right\rangle. \quad (2)$$

In (1) and (2), angle brackets denote averaging in horizontal planes at constant values of the wave following coordinate ζ , $(\tau_{1k}; \tau_{ck})$ are subgrid-scale turbulence terms, W is the contravariant vertical flux velocity, z_t is the grid speed, J is the Jacobian of the mapping transformation from physical to computational space, and $\partial \zeta / \partial x_k$ are grid metrics. These equations are obtained from the strong conservation form of the governing transport equations and thus satisfy a global flux balance over the computational domain (see Sullivan et al. (2014) for a detailed derivation of these equations). (1) and (2) are similar but differ critically in their vertical flux composition. The streamwise momentum flux contains three terms, viz., pressure-wave slope correlation (form drag at the water surface), resolved turbulence and subgrid-scale turbulence while the vertical flux in the scalar equation contains only resolved and subgrid-scale turbulence terms, there is no pressure contribution. Fig. 27 shows vertical profiles of the individual flux components and their sum for momentum and scalar concentration. For our simulations, the total momentum and scalar fluxes are nearly constant over a vertical extent of $\sim 0.06\lambda$ above the water surface. The important difference is the large pressure contribution to the total stress in the constant flux layer, nearly 75% in the case with active breaking. With breaking waves, a large fraction of the total drag is due to pressure drag, with the resolved and subgrid-scale turbulence becoming a smaller fraction of the total. However the scalar exchange is always determined by the turbulent surface layer winds, essentially the resolved and subgrid-scale terms in (2), which in our flows are significantly reduced by breaking waves. Hence these simulation results highlight fundamental and important differences between momentum and scalar surface exchange over a moving wave field with strong air-side separation, such as occurs during wave breaking.

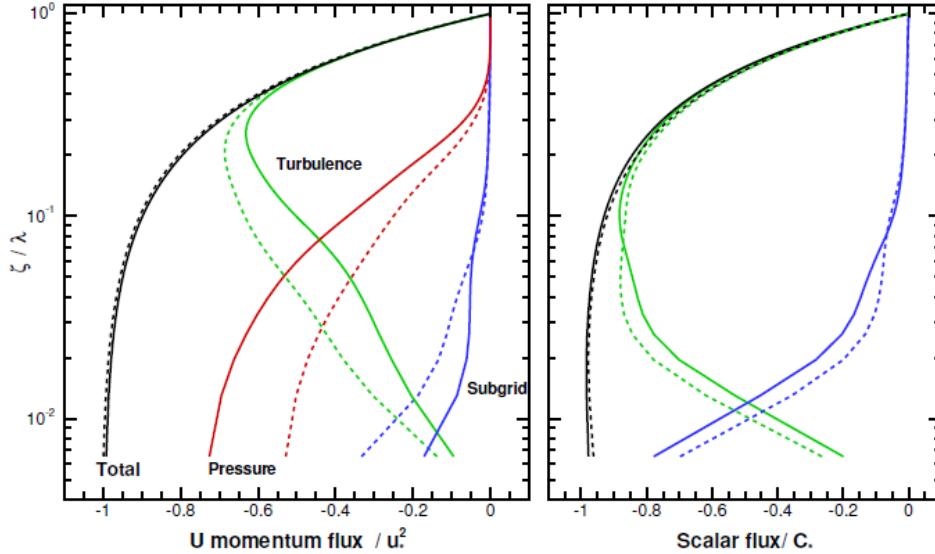


Figure 27. Vertical profiles of the terms in the ensemble average streamwise momentum (left panel) and scalar (right panel) budgets computed in LES wave-following coordinates. Flow over incipient and active breakers is indicated by dashed and solid lines, respectively. The contributions to the streamwise momentum flux are: pressure-wave slope correlation (form drag) $p\zeta_x/J$ (red curves), vertical turbulent momentum flux $u(W - z_t)$ (green curves), and the subgrid-scale flux (blue curves). Contributions to the average scalar flux are: vertical turbulent scalar flux $C(W - z_t)$ (green curve) and the subgrid-scale flux (blue curve). In each panel the total flux is shown by black curves. Momentum and scalar fluxes are normalized by the total stress u_*^2 and surface flux C_* , respectively. Results are obtained using a fine grid of $(512 \times 512 \times 128)$ points.

Auxiliary flow visualization measurements

We also undertook a series of flow visualization studies at the UNSW Water Research Laboratory to complement the LES results, particularly to validate the interesting conclusion from the LES that the surface velocity boundary condition has little impact on the flow separation phenomenon – its occurrence rate, horizontal and vertical extent compared with maximally steep unbroken waves.

A schematic of the wind-wave flume is shown in Fig. 28 below. The wind tunnel working section was 4m long, 0.6 m wide and 0.5 m high. A 300 mW laser expanded through a cylindrical lens to produce a light sheet that was beamed downward through an access slot in the wind tunnel roof. It illuminated a vertical triangular area approximately 1 m in length at the waterline along the tank centreline. The wind flow produced by an adjustable speed suction fan system was suitably seeded with particles from a smog generator machine, introduced upstream of the honeycomb section.

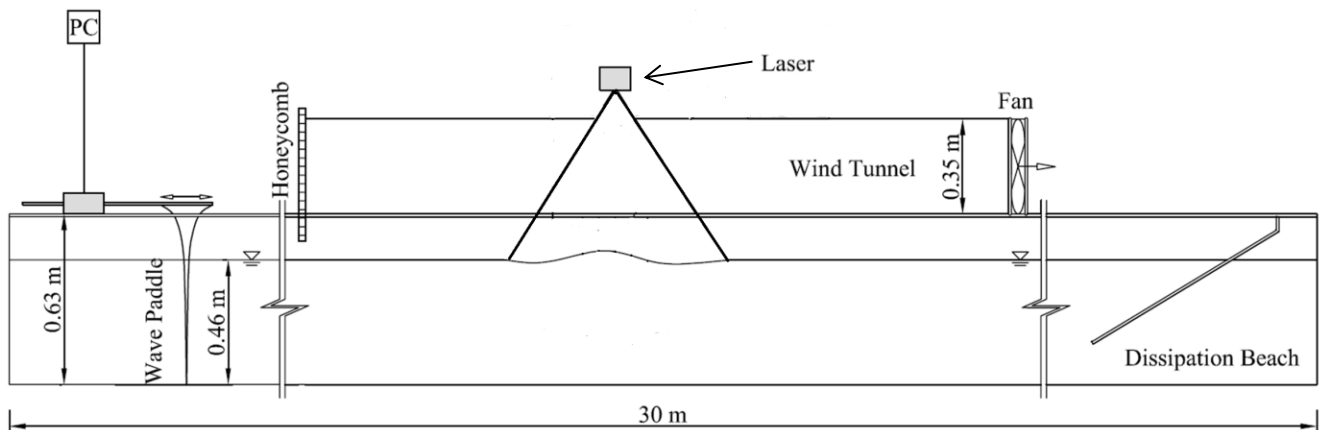
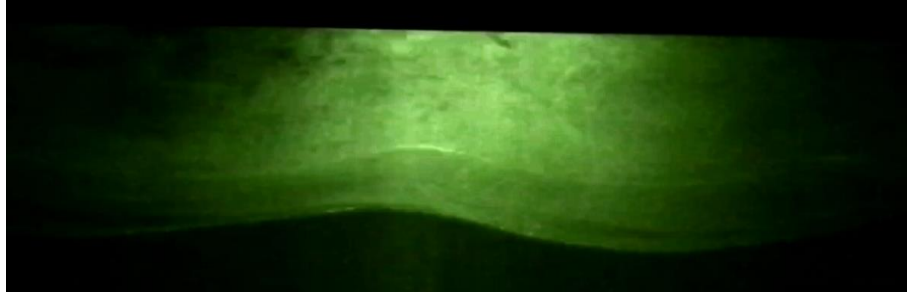


Figure 28. Schematic of wind wave facility flow used for our flow visualization study.

Paddle-generated steep uniform wave trains and modulated packets were investigated, with flow speed ratios U_{ref}/c spanning the range 0.8 to 3, above which the smog particle density became too low for capturing useful imagery. Two camera systems were used to gather video imagery: (i) a SONY $\alpha 7\text{RII}$ operating at 60 Hz frame rate at 1080P resolution (ii) an IPHONE 7 operating in SLO-MO capability at 120 Hz frame rate at 1080P resolution and 240 Hz frame rate at 720P resolution.

The flow visualisation study was undertaken to complement the LES findings and provide additional insights into the key issue as to what features of the wave geometry might control the onset of flow separation. Identifying the flow separation and recirculation is far easier in the video where you can see the motion rather than in a sequence of still frames. Available evidence (Giovanangeli et al., 1999) up to intermediate wave slopes suggests a linear correlation with wave steepness and with wave age. While of interest, such parametric correlations do not address the key determinant(s), especially the issue whether breaking has a special role in the process. Our aim is to learn whether a more refined measure of the surface geometry, such as local crest curvature, or time rate of change of slope, needs to be monitored in order to properly characterize this important aspect of wind-wave interaction. We are continuing to investigate this in conjunction with the still-ongoing LES collaborative study with P. Sullivan at NCAR, where we are also examining comparisons of the visual character of the LES flow field with the wave tank visualizations.

Attached air flow – no separation:



Air flow separation:

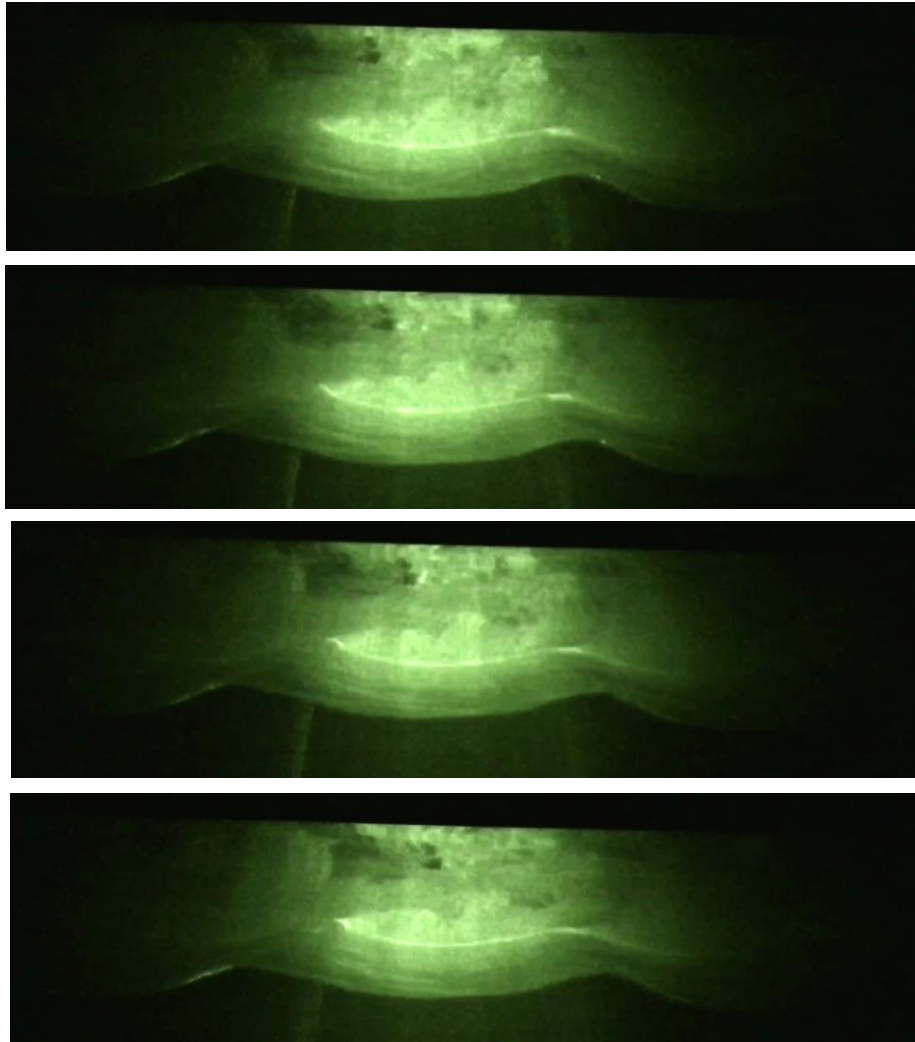


Figure 29. Images from the laboratory flow visualization over steep modulating paddle-initiated wind-driven waves. Top panel: typical attached flow (no separation) over steep, non-breaking wave. Following panels: wave shown enters the frame on the left, starting to break. It is seen that the smoke particles are trapped in the (brighter) separation bubble in the trough just downwind of the crest. The same wind flowing over a subsequent comparably steep, but non-breaking wave shows no evidence of separation. The wind and wave directions are from left to right. The wind speed $U_{ref} \sim 1.95$ m/s, the wave speed $c \sim 0.62$ m/s hence $U_{ref}/c \sim 3$. Time increases from top to bottom, with 1/120 sec. intervals between each frame.

Upscaling to Ocean Conditions at Very High Windspeeds

For the purposes of the present discussion, typical wind speeds U_{ref} for gale force to hurricane strength winds are 20 – 50 m/s, with dominant ocean wavelengths spanning the range 150 - 300 m. Therefore there are formidable difficulties associated with obtaining direct measurements of the aerodynamics of wind flow over ocean waves forced by gale force and even stronger winds. Hence insights gained from extrapolating LES results can provide potentially relevant guidance for the extreme field conditions provided that upscaling can be justified.

From dimensional arguments, the non-dimensional parameters that need to be respected in the upscaling are the dominant wave steepness (AK), the wave age (c/U_{ref}) and in principle, the representative Reynolds number $U_{\text{ref}} * L_{\text{ref}}/\nu$ and the spectral bandwidth of the wave field. The representative wave speed c , length scale L_{ref} and wind speed U_{ref} are conveniently taken as the spectral peak phase speed and wavelength, and wind speed at height $L_{\text{ref}}/2$ above mean sea level. The representative wave height A is often taken as half the significant wave height H_s .

To make open ocean inferences from our LES study of our very steep young laboratory waves, conserving the dominant wave steepness AK is seen as a minimum requirement, given the sensitivity to wave steepness found in the LES study. Conserving the age (c/U_{ref}) of the dominant waves should (all other factors being equal) result in similar mean streamline patterns in the air at different scales, so the sheltering effects identified for laboratory scale flows should be operative. Matching dominant wave steepness AK and wave age (c/U_{ref}) enables us to extend our laboratory/LES cases in relation to naturally-observed fetch/duration limited oceanic conditions for pure wind seas, in the absence of swell. Further guidance, related to upscaling, is provided by the Toba (1972) empirical similarity relation:

$$H_s = B (gu_*)^{1/2} T_s^{3/2}$$

for the relationship between significant wave height H_s and significant wave period T_s over a wide range of wave age conditions, from wave tanks to ocean waves forced by winds up to gale force strength, where the empirical constant $B \sim 0.62$ (Bailey et al., 1991). In the present context, the Banner (1990) data for breaking waves sits on the Toba curve at the very young laboratory wave extreme. Recently, Savelyev et al. (2011) revisited this empirical constraint and re-expressed it in terms of U_{ref} . This is more suitable for our present upscaling considerations as the wind speed is intrinsic to the wave scale, specified typically at a nominal fraction of the dominant wave length, rather than the friction velocity:

$$AK = 0.082 (U_{\text{ref}}/c)^{1/2}.$$

Here U_{ref} , c and AK are the reference wind speed, phase speed and mean steepness of the dominant wind waves. We note that Toba's relation degrades for swell interacting with wind-sea, which can modify both the swell and wind sea, and which needs to be taken into account when upscaling.

Feasibility of upscaling results from our very strongly forced young waves LES simulations to gale force - hurricane strength winds.

It is assumed that laboratory measurements that emulate air-sea interfacial boundary layer flows are undertaken at a Reynolds number sufficient to guarantee fully-rough turbulent flow. Based on the wavelength and U_{ref} the tank Reynolds number for the wind flow $\sim 2.5 \times 10^4$ whereas it is $\sim 10^6$ for the very strongly forced ocean case. However, both are nominally in the 'fully turbulent' range.

The spectral bandwidth of the waves is another key issue. This has conceptual as well as hydrodynamical and aerodynamical implications. It obscures wave age based on u_* (depends on

integration of all spectral contributions) and wave age based on U_{ref} , which is arguably more directly comparable for upscaling purposes. In Banner (1990), the dominant breaking waves had $U_{\text{ref}}/c \sim 10$, $AK \sim 0.27$. According to Toba's relation, at $U_{\text{ref}} = 50$ m/s, the extrapolated wave speed for this same extreme steepness would have $c = 5$ m/s, corresponding to waves with 15 m wavelength. These would be very transient as rapidly developing young dominant waves, but plausibly far more persistent as shorter roughness elements in the tail of a much more developed, broader wave spectrum with peak wavelengths of $O(200-300)$ m. In that role, our simulations indicate that these very steep unsteady wave packets could have a strong effect on the wave drag in the spectral tail and hence on the total drag. Their net contribution would depend on their statistics, which to date is not well-known. In view of the strong net contribution from unsteadiness found here, this aspects warrant further study.

Another important factor related to the wave spectral bandwidth is the attenuation of short wind waves by steep dominant waves. This is a very strong effect in laboratory experiments, where it has been known since the 1970's (Phillips and Banner, 1974, Donelan, 1987, Chen and Belcher, 2000). The precise causal mechanism is still being argued. It is far more difficult to isolate the effect in field data, but despite receiving some attention over the past decade (e.g. García-Nava H. et al, 2009, 2012), it is not yet reconciled as to whether this effect is operative to anywhere near the levels observed for laboratory scales. This is primarily because of the strong dependence of the short wave attenuation on dominant wave steepness. Improved observational remote sensing capabilities for observing short waves in the field, such as polarimetric cameras (e.g. Zappa et al., 2013) now offer the potential to elucidate this further in strongly forced, high sea states in the field.

Kelvin-Helmholtz instabilities may also play a significant role in influencing the dynamics at the air-sea interface in very strong wind conditions. Soloviev and Lukas (2006) introduced the Koga number as the criterion for this type of instability at the air-sea interface. The Koga number characterizes the ratio between the velocity difference across the aqueous viscous sublayer and the minimum phase speed of gravity capillary waves, which takes into account surface tension and gravity forces that work to prevent the air-sea interface from disruption. The change of the air-sea interaction regime in hurricane conditions has been linked to the direct disruption of the air-sea interface by pressure fluctuations working against the surface tension, through Kelvin-Helmholtz instability. Due to restrictions in our LES computational method these effects were not considered in our present study.

INTERIM SUMMARY OF MAJOR FINDINGS

In our LES modeling study of very strongly forced young waves, where the reference wind speed is up to ten times the wave speed, flow separation characterizes the wind over propagating steep wave forms with fixed shape. A controlling influence is confirmed to be geometrical steepness rather than the imposed kinematic boundary condition for the fluid speed along the boundary, as was previously assumed to be an important factor. We added a sinusoidal surface wind drift distribution with a mean level of $0.03 U_{\text{ref}}$ to the wave orbital velocities wherein the fluid velocity reached the wave crest speed at the crest. This produced only a small increase in the mean wind speed profile over the waves, with a corresponding small reduction in the wave form drag fraction of the wind stress. These findings are consistent with the latest theoretical perspectives on flow separation that indicate very different conditions for flow separation over rigid surfaces compared with unsteady surfaces with a boundary slip velocity (e.g. see Miron & Vétel, 2015).

Our steady breaker LES results also highlight important fundamental differences between momentum and scalar surface exchange over a moving wave field where the wind flow separates over steep wave crests. This appears to be operative during wave breaking events, primarily because of the large geometric steepness. It is well known that in turbulent flow over steep stationary roughness, the primary mechanism for transferring momentum to the underlying surface is via pressure drag resulting

from flow separation whereas scalar transfer is determined largely by viscous processes. Flow separation in wave troughs is accompanied by weak surface wind recirculation which is inefficient at transferring scalars between the underlying wavy surface and the overlying air flow. As a result, we found that the effective surface roughness differ fundamentally for momentum and for scalars over steep, breaking waveforms with separated air flow. These results need further investigation for high winds over a spectrum of waves where flow separation can occur at multiple scales.

Strongly-forced wind seas are characterized by enhanced group modulation, as significant additional energy flux from the wind augments the hydrodynamic modulations. We investigated for the first time the aerodynamic consequences of strong temporal and spatial group structure (modulation), by introducing compact, steep but non-breaking, chirped wave packets into the LES study. These packets, generated by our fully nonlinear boundary element wave code, added strong temporal and spatial variability similar in character to that observed in strongly forced wind sea. The inclusion of unsteadiness in the surface geometry added transient large steepness events to the LES, which produced strong air flow perturbations, especially those associated with the resulting air flow separation. These disturbances can penetrate vertically to significant elevations above the waves and make disproportionately large local stress spikes that add significant increments to the *mean* stress. These findings signal the potential value in augmenting the classical measure of wave steepness to better diagnose the occurrence of air flow separation, which can produce large changes to the form drag and total drag. Given the complex surface behavior of the aerodynamics over unsteady steep wave forms, analysis of these LES results is still in progress to provide insights into the mechanism(s) underpinning air flow separation and will be reported in the Final Technical Report for this project. These findings point to the need for more refined knowledge of modulational properties of the wave field in order to provide more accurately quantify air-sea fluxes, especially during strong wind forcing events.

Finally, we investigated the scope for upscaling these results to ocean conditions. There are a number of related aspects that impact on up-scalability. As the wave spectral bandwidth is much broader in the field than in the laboratory, the fundamental aerodynamic phenomena have a strong counterpart, especially for the steeper short wave scales. The wave spectral bandwidth introduces additional complexity including long wave-short wave interactions and modulation, which can potentially have a strong impact on the wave spectrum and on the surface fluxes. There are also additional key physical mechanisms that come into play under very strong wind forcing and were not taken into account in our study. These include: spray and large droplet production associated with breaking wave crests and even crest disintegration through shearing at the highest wind speeds. These aspects will be discussed further in the Final Technical Report for the project.

IMPACT/APPLICATIONS

This project provides an assessment of the likely impacts of steep wave geometry and surface kinematics on air-sea fluxes of momentum and scalar transfers for very strongly-forced young wind sea conditions. Such conditions arise where the reference wind speed is an order of magnitude faster than the wave speed. These conditions occur during the initial rapid buildup of the sea state as severe winds accelerate, or during sustained storm events for short waves beyond the spectral wave peak, where these steep short wave scales are riding on much longer, less steep dominant waves. While the wind is still modulated by these dominant waves, they will cause far less flow separation, and the aerodynamic results found here for the shorter-scale riding waves will likely be applicable much of the time. The unknown factor is to what extent the dominant seas ‘iron out’ the shorter wave scales, as discussed above under ‘upscalability’. To advance present knowledge, these aspects will require future observational investigation on this a long-standing knowledge gap, which is an important factor underpinning the behavior of the sea surface drag coefficient for gale force and higher wind speeds.

PUBLICATIONS

- Saket, Arvin, William L. Peirson, Michael L. Banner, Xavier Barthelemy and Michael Allis, 2016: Wave breaking onset of two-dimensional deep-water wave groups in the presence and absence of wind. *J. Fluid Mech.* DOI: <https://doi.org/10.1017/jfm.2016.776>. Published online: 15 December 2016 [published, refereed]
- Christopher J. Zappa, Michael L. Banner, Russel P. Morison, Sophia E. Brumer, 2016: On the Variation of the Effective Breaking Strength in Oceanic Sea States, *J. Phys. Oceanogr.*, *46*, 2049-2061. DOI: <http://dx.doi.org/10.1175/JPO-D-15-0227.1> [published, refereed]
- Michael L. Banner and Russel P. Morison, 2015: On the Upper Ocean Turbulent Dissipation Rate due to Very Short Breaking Wind-Waves. *arXiv*:1602.06649 [published]
- X. Barthelemy, M.L. Banner, W.L. Peirson, F. Dias and M. Allis, 2015: On the local properties of highly nonlinear unsteady gravity water waves. Part 1. Slowdown, kinematics and energetics. *arXiv*:1508.06001 [published]
- X. Barthelemy, M.L. Banner, W.L. Peirson, F. Fedele, M. Allis and F. Dias, 2015: On the local properties of highly nonlinear unsteady gravity water waves. Part 2. Dynamics and onset of breaking. *arXiv*:1508.06002 [published]
- M.L. Banner, X. Barthelemy, F. Fedele, M. Allis, A. Benetazzo, F. Dias and W.L. Peirson, 2014: Linking reduced breaking crest speeds to unsteady nonlinear water wave group behavior. *Phys. Rev. Lett.* *112*, 114502. [published, refereed]
- M.L. Banner, C.J. Zappa and J.R. Gemmrich, 2014: A note on the Phillips spectral framework for ocean whitecaps. *J. Phys. Oceanogr.*, *44*, 1727–1734. [published, refereed]
- W.L. Peirson, J.W. Walker and M.L. Banner, 2014: On the microphysical behaviour of wind-forced water surfaces and consequent re-aeration. *J. Fluid Mech.* *743*, 399-447. [published, refereed]
- W.L. Peirson, J.F. Beyá, M.L. Banner, J.S.Peral and S.A. Azarmsa, 2013. Rain-induced attenuation of deep-water waves. *J. Fluid Mech.*, *724*, 5-35. doi:10.1017/jfm.2013.87 [published, refereed]
- H.L. Tolman, M.L. Banner and J.M. Kaihatu, 2013. The NOPP operational wave model improvement project. *Ocean Modelling*, *70*, 2-10. <http://dx.doi.org/10.1016/j.ocemod.2012.11.011> [published, refereed]
- J.R. Gemmrich, C.J. Zappa, M.L. Banner and R.P. Morison, 2013. Wave breaking in developing and mature seas. *J. Geophys. Res. Oceans*, *241*, 118, 4542 – 4552, doi: 10.1002/jgrc.20334. [published, refereed]
- C.J. Zappa, J.R. Gemmrich, R.P. Morison, H. Schultz, M.L. Banner, D.A. LeBel, and T. Dickey. 2012. An overview of sea state conditions and air-sea fluxes during RaDyO, *J. Geophys. Res. Oceans*, doi:10.1029/2011JC007336. [published, refereed]
- X. Barthelemy, M.L. Banner, W.L. Peirson, F. Fedele, M. Allis, F. Dias, 2015: On the local properties of highly nonlinear unsteady gravity water waves. Part 2. Dynamics and onset of breaking. *arXiv*:1508.06002 [published]
- Peirson, W.L., Beya, J.F., Banner, M.L., Peral, J.S. and Azarma, S.A., 2013: Rain-induced attenuation of water waves. *J. Fluid Mech.* *724*, 5-35. [published, refereed]
- Schnieders, J., Garbe, C. S., Peirson, W. L., Smith, G.B., and Zappa, C. J., 2013: Analyzing the footprints of near surface aqueous turbulence – an image processing based approach. *J. Geophys. Res. C:Oceans* *118* (3), 1272-1286. [published, refereed]
- Grare, L., Peirson, W.L., Branger, H., Walker, J.W., Giovanangeli, J-P, Makin, V.K., 2013: Growth and dissipation of wind-forced, deep water waves. *J. Fluid Mech.* *722*, 5-50. [published, refereed]
- Blenkinsopp, C.E., Allis, M.J., Turner, I.L., Peirson, W.L. and Gerden, L., 2012: Application of LiDAR technology for measurement of time-varying free-surface profiles in a laboratory wave flume. *Coastal Eng.*, *68*, 23-38. [published, refereed]

- Beya, J.F., Peirson, W.L. and Banner, M.L., 2012: Transport and turbulence beneath finite amplitude water waves. *Expt. in Fluids*, **52**, 1319 - 1330. DOI 10.1007/s00348-011-1254-4. [published, refereed]
- Beya, J.F., Peirson, W.L., Banner, M.L. (2011) Rainfall-generated, near-surface turbulence. In *Gas Transfer at Water Surfaces*. Eds. S. Komori, W. McGillis and R. Kurose. Kyoto University Press. ISBN 978-4-87698-560-9. pp. 90-103 [published, refereed]
- Yan, X., Peirson, W.L., Walker, J.W., Banner, M.L., 2011: On transitions in the Schmidt number dependency of low solubility gas transfer across air-water interfaces. In *Gas Transfer at Water Surfaces*. Eds. S. Komori, W. McGillis and R. Kurose. Kyoto University Press ISBN 978-4-87698-560-9, pp333-343 [published, refereed]

REFERENCES

- Adrian, R. J., 2007: Hairpin vortex organization in wall turbulence, *Phys. Fluids*, **19**, 041301.
- Bailey, Richard J., Ian. S.F. Jones and Yoshiaki Toba, 1991: The steepness and shape of wind waves. *J. Oceanogr. Soc. Japan*, **47**, 249-264.
- Banner, M.L. & Melville, W.K., 1976: On the separation of air flow over water waves. *J. Fluid Mech.* **77**, 825–842.
- Banner, M. L., 1990: The influence of wave breaking on the surface pressure distribution in wind-wave interaction. *J. Fluid Mech.*, **211**, 463–495.
- Banner, M.L., X. Barthelemy, F. Fedele, M. Allis, A. Benetazzo, F. Dias and W.L. Peirson, 2014. Linking reduced breaking crest speeds to unsteady nonlinear water wave group behavior. *Phys. Rev. Lett.*, **112**, 114502.
- Barthelemy, X., M.L. Banner, W.L. Peirson, F. Fedele, M. Allis and F. Dias, 2015: On the local properties of highly nonlinear unsteady gravity water waves. Part 2. Dynamics and onset of breaking. *arXiv:1508.06002*.
- Black, P., E. D'Asaro, W. Drennan, J. French, P. Niiler, T. Sanford, E. Terrill, E. Walsh and J. Zhang, 2007: Air-sea exchange in hurricanes: Synthesis of observations from the Coupled Boundary Layers Air-Sea Transfer experiment. *Bull. Amer. Meteorol. Soc.*, **88**, 357–374.
- Buckley, M.P. and Veron, F. 2016: Structure of the airflow above surface waves. *J. Phys. Oceanogr.*, **46**, 1377-1397
- Cebeci, T. & P. Bradshaw, 1988: physical and computational aspects of convective heat transfer, Springer-Verlag, p.487.
- Chen, G., and S. E. Belcher, 2000: Effects of long waves on wind generated waves, *J. Phys. Oceanogr.*, **30**, 2246–2256.
- Donelan, M.A., 1987: The effect of swell on the growth of wind waves, Johns Hopkins APL Tech. Dig., **8**(1), 18–23.
- French, J. R., D. W. M, J. A. Zhang, and P. G. Black, 2007: Turbulent fluxes in the hurricane boundary layer. Part i: Momentum flux. *J. Atmos. Sci.*, **64**, 1089–1102.
- García-Nava H., Ocampo-Torres F. J., Osuna P., Donelan M.A., 2009: Wind stress in the presence of swell under moderate to strong wind conditions. *J. Geophys. Res.* **114**: C12008.
- García-Nava, H., F.J. Ocampo-Torres, P.A. Hwang, and P. Osuna, 2012: Reduction of wind stress due to swell at high wind conditions. *J. Geophys. Res.*, **117**, C00J11, doi:10.1029/2011JC007833
- Gent, P. R. and P. A. Taylor, 1977: A note on 'separation' over short wind waves. *Boundary-Layer Meteorol.*, **11**, 105–128.
- Giovanangeli, J.P., N. Reul, M. Garat & H. Branger. 1999: Some Aspects of Wind-Wave Coupling at High Winds: an Experimental Study. In 'Wind-Over-Wave Couplings', Eds. S.G. Sajjadi, N.H. Thomas & J.C.R. Hunt, Clarendon Press, 81-90.
- Jessup, A.T. & K.R. Phadnis, 2005: Measurement of the geometric and kinematic properties of microscale breaking waves from infrared imagery using a PIV algorithm. *Meas. Sci. Technol.* **16**, 1961–1969.

- Large, W. G. and S. Pond, 1981: Open ocean flux measurements in moderate to strong winds. *J. Phys. Oceanogr.*, 11, 324–336.
- Miron, Philippe and Jérôme Vétel, 2015: Towards the detection of moving separation in unsteady flows. *J. Fluid Mech.*, 779, 819–841 doi:10.1017/jfm.2015.461
- Phillips, O.M., and M.L. Banner, 1974: Wave breaking in the presence of wind drift and swell, *J. Fluid. Mech.*, 66, 625–640.
- Powell, M. D., P. J. Vickery, and T. A. Reinhold, 2003: Reduced drag coefficient for high wind speeds in tropical cyclones. *Nature*, 422, 279–283.
- Rapp, R. J. & Melville, W.K., 1990: Laboratory measurements of deep-water breaking waves. *Phil. Trans. R. Soc. Lond. A* **331**, 735–800.
- Reul, N., H. Branger, and J.-P. Giovanangeli, 2007: Air flow structure over short-gravity breaking waves. *Boundary-Layer Meteorol.*, 126, 477–505.
- Richter, D. H., and P. P. Sullivan, 2013a: Momentum transfer in a turbulent, particle-laden Couette flow. *Phys. Fluids*, 25, 053304, doi:10.1063/1.4804391.
- Richter, D. H., and P. P. Sullivan, 2013b: Sea surface drag and the role of spray. *Geophys. Res. Lett.*, 40, 656–660, doi:10.1002/grl.50163.
- Savelyev, I., B. K. Haus and M. A. Donelan. 2011: Experimental study on wind-wave momentum flux in strongly forced conditions”, *Journal of Physical Oceanography*, 41, 1328-1344.
- Soloviev, A., R. Lukas, M. Donelan, B. Haus, and I. Ginis, 2014: The air-sea interface and surface stress under tropical cyclones. *Nature.com/Scientific Reports* 4, 5306.
- Stansell, Paul & MacFarlane, C., 2002: Experimental investigation of wave breaking criteria based on wave phase speeds. *J. Phys. Oceanogr.*, 32, 1269–1283.
- Sullivan, P. P., J. C. McWilliams & C-H. Moeng, 2000: Simulation of turbulent flow over idealized water waves. *J. Fluid Mech.* 404, 47-85.
- Sullivan, P. P. and J. C. McWilliams, 2002: Turbulent Flow over water waves in the presence of stratification. *Physics of Fluids*, 14, 1182-1195.
- Sullivan, P. P., J. C. McWilliams & W. K. Melville, 2004: The oceanic boundary layer driven by wave breaking with stochastic variability. I: Direct numerical simulations. *J. Fluid Mech.*, 507, 143–174.
- Sullivan, P. P., J. B. Edson, T. Hristov, and J. C. McWilliams, 2008: Large eddy simulations and observations of atmospheric marine boundary layers above non-equilibrium surface waves. *J. Atmos. Sci.*, 65, 1225–1245.
- Sullivan, P. P. and J. C. McWilliams, 2010: Dynamics of winds and currents coupled to surface waves. *Ann. Rev. Fluid Mech.*, 42, 19–42.
- Sullivan, P.P., J.C. McWilliams and T. Hristov, 2010a: A large eddy simulation model of high wind marine boundary layers above a spectrum of resolved moving waves. 19th Amer. Meteorol. Soc. Symp. on Boundary Layer and Turbulence, Keystone, CO.
- Sullivan, P. P., J. C. McWilliams and E. G. Patton, 2014: Large eddy simulation of marine atmospheric boundary layers above a spectrum of moving waves. *J. Atmos. Sci.*, 71, 4001-4027.
- Veron, F., G. Saxena, and S. K. Misra, 2007: Measurements of the viscous tangential stress in the airflow above wind waves. *Geophys. Res. Lett.*, 34, L19603.
- C.J. Zappa, J.R. Gemmrich, R.P. Morison, H. Schultz, M.L. Banner, D.A. LeBel, and T. Dickey. 2012. An overview of sea state conditions and air-sea fluxes during RaDyO, *J. Geophys. Res. Oceans*, doi:10.1029/2011JC007336.
- Zhou, J., R. J. Adrian, S. Balachandar, and T. M. Kendall, 1999: Mechanisms for generating coherent packets of hairpin vortices in channel flow, *J. Fluid Mech.*, 387, 353–396.